



Transformative Advances in DDDAS with Application to Space Weather Monitoring

Dennis Bernstein
UNIVERSITY OF MICHIGAN

10/01/2015
Final Report

DISTRIBUTION A: Distribution approved for public release.

Air Force Research Laboratory
AF Office Of Scientific Research (AFOSR)/ RTA2
Arlington, Virginia 22203
Air Force Materiel Command

DISTRIBUTION A: Distribution approved for public release.

REPORT DOCUMENTATION PAGE			Form Approved OMB No. 0704-0188	
<p>The public reporting burden for this collection of information is estimated to average 1 hour per response, including the time for reviewing instructions, searching existing data sources, gathering and maintaining the data needed, and completing and reviewing the collection of information. Send comments regarding this burden estimate or any other aspect of this collection of information, including suggestions for reducing the burden, to Department of Defense, Executive Services, Directorate (0704-0188). Respondents should be aware that notwithstanding any other provision of law, no person shall be subject to any penalty for failing to comply with a collection of information if it does not display a currently valid OMB control number.</p> <p>PLEASE DO NOT RETURN YOUR FORM TO THE ABOVE ORGANIZATION.</p>				
1. REPORT DATE (DD-MM-YYYY) 19-10-2015	2. REPORT TYPE Final Performance	3. DATES COVERED (From - To) 01-09-2012 to 14-10-2015		
4. TITLE AND SUBTITLE Transformative Advances in DDDAS with Application to Space Weather Monitoring			5a. CONTRACT NUMBER	
			5b. GRANT NUMBER FA9550-12-1-0401	
			5c. PROGRAM ELEMENT NUMBER 61102F	
6. AUTHOR(S) Dennis Bernstein			5d. PROJECT NUMBER	
			5e. TASK NUMBER	
			5f. WORK UNIT NUMBER	
7. PERFORMING ORGANIZATION NAME(S) AND ADDRESS(ES) UNIVERSITY OF MICHIGAN 503 THOMPSON ST ANN ARBOR, MI 48109-1340 US			8. PERFORMING ORGANIZATION REPORT NUMBER	
9. SPONSORING/MONITORING AGENCY NAME(S) AND ADDRESS(ES) AF Office of Scientific Research 875 N. Randolph St. Room 3112 Arlington, VA 22203			10. SPONSOR/MONITOR'S ACRONYM(S) AFRL/AFOSR RTA2	
			11. SPONSOR/MONITOR'S REPORT NUMBER(S)	
12. DISTRIBUTION/AVAILABILITY STATEMENT A DISTRIBUTION UNLIMITED: PB Public Release				
13. SUPPLEMENTARY NOTES				
14. ABSTRACT This project focused on DDDAS-motivated developments in support of space weather monitoring and prediction. The project involved four interrelated tasks relating to physics-driven adaptive modeling, adaptive data assimilation with input reconstruction, event-based sensor reconfiguration, and optimization of scheduling. For data assimilation, the emphasis has been on model refinement. The problem of estimating the eddy diffusion coefficient using total electron content measurements has led to new techniques for determining the essential modeling details needed by the retrospective cost model refinement technique. For spacecraft design, multidisciplinary optimization design techniques were applied to the design of small satellites accounting for multiple vehicle subsystems. For download scheduling, optimization techniques were used to account for multiple spacecraft and ground stations				
15. SUBJECT TERMS DDDAS				
16. SECURITY CLASSIFICATION OF: a. REPORT Unclassified		b. ABSTRACT Unclassified	c. THIS PAGE Unclassified	17. LIMITATION OF ABSTRACT UU
			18. NUMBER OF PAGES UU	19a. NAME OF RESPONSIBLE PERSON Dennis Bernstein
				19b. TELEPHONE NUMBER (Include area code) 734-764-3719

Standard Form 298 (Rev. 8/98)
 Prescribed by ANSI Std. Z39-18

DISTRIBUTION A: Distribution approved for public release.

Transformative Advances in DDDAS with Application to Space Weather Monitoring

AFOSR DDDAS Grant FA9550-12-1-0401

Final report submitted to

Frederica Darema, AFOSR
September 28, 2015

Dennis S. Bernstein, Principal Investigator
Department of Aerospace Engineering
The University of Michigan
Ann Arbor MI, 48109-2140
(734) 764-3719
dsbaero@umich.edu

Co-Investigators: Aaron Ridley, Jamie Cutler, Amy Cohn

Abstract

This project focused on DDDAS-motivated developments in support of space weather monitoring and prediction. The project involved four interrelated tasks relating to physics-driven adaptive modeling, adaptive data assimilation with input reconstruction, event-based sensor reconfiguration, and optimization of scheduling. For data assimilation, the emphasis has been on model refinement. The problem of estimating the eddy diffusion coefficient using total electron content measurements has led to new techniques for determining the essential modeling details needed by the retrospective cost model refinement technique. For spacecraft design, multidisciplinary optimization design techniques were applied to the design of small satellites accounting for multiple vehicle subsystems. For download scheduling, optimization techniques were used to account for multiple spacecraft and ground stations.

1 Project Objectives

Space weather can have a catastrophic effect on operational satellites and ground systems. The ability to monitor space weather is thus important to both the U.S. civilian and military infrastructure. With this motivation in mind, this project addresses aspects of each of the four DDDAS science and technology Frontiers. For the Applications Modeling Frontier, we consider *physics-driven adaptive modeling*, where current conditions elicit the need for an appropriate physics model. For the Mathematical and Statistical Algorithms Frontier, we consider *adaptive data assimilation with input reconstruction*, where the ability to reconstruct inputs can enhance the ability to estimate the state of a system and improve the accuracy of the underlying model. For the Application Measurement Systems and Methods Frontier we consider *event-based sensor reconfiguration*, where a measurement system modifies its functionality based on operational priorities. For the Advances in Systems Software Frontier we consider *hierarchical closed-loop scheduling*, where communication links and their constraints are accounted for in both autonomous agent-based and centralized software systems.

2 Summary of Main Results

2.1 Model Refinement and Input Reconstruction

For modeling the ionosphere-troposphere, we use the Global Ionosphere-Thermosphere Model [77], which is a CFD code with atmospheric chemistry, as the basis for data assimilation, input estimation, and subsystem identification. These objectives were addressed by applying a specialized technique that is being developed under this project. This technique is called retrospective-cost-based adaptive input and state estimation (RCAISE). We applied RCAISE to GITM in order to estimate unknown drivers (inputs) to the ionosphere-thermosphere [2, 24]. This approach complements ensemble-based methods as in [66], which applies the ensemble code DART to GITM, since the main goal of RCAISE is to estimate the unknown input rather than obtain estimates of all model states. Since RCAISE is not an ensemble code, it is highly computationally efficient compared to DART, but, unlike DART, it provides best estimates rather than a probability density function. A related approach was previously demonstrated in [25] to identify a subsystem cooling model whose dynamics are inaccessible in the sense that neither the input nor the output of the cooling subsystem dynamics are measured.

Much of this effort has focused on determining the essential modeling details required by RCAISE for both input estimation and model refinement. For linear systems, this information is well understood. However, for application to space weather modeling, GITM is both extremely nonlinear and high dimensional. Our goal is thus to extract the essential modeling details from numerical simulations. For earlier studies, numerical testing was used to determine this information. However, an additional goal was to estimate the eddy diffusion coefficient (EDC) using total electron content (TEC) data. TEC data is available from ground stations located worldwide, and thus RCAISE is able to work with multiple measurements. Numerical testing has shown that estimating this modeling information is computationally expensive, and thus more efficient methods are needed.

In previous work, RCMR was used in [25] to estimate NO_x cooling profile using GITM and simulated spacecraft measurements. This study was limited to a one-dimensional version of GITM. RCMR was subsequently used in [18] to estimate the photoelectron heating coefficient in a fully three-dimensional version of GITM using both simulated and real satellite measurements. The applications in [25] and [18] demonstrated the ability of RCMR to adaptively refine a nominal model by iteratively updating an estimate of an unknown parameter modeled by an adaptive subsystem model. This parameter is modeled as an unknown

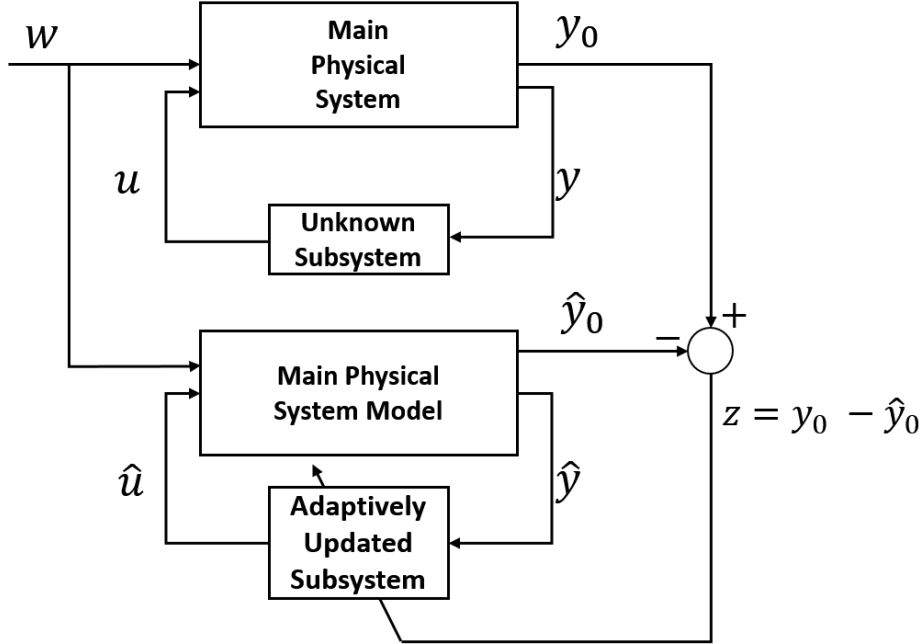


Figure 1: Retrospective Cost Model Refinement (RCMR) architecture. The main physical system is interconnected by means of feedback with an unknown subsystem that models the uncertainty in the physical system. RCMR uses the model output error $z \triangleq y_0 - \hat{y}_0$ to adjust the adaptive subsystem model to estimate the unknown subsystem. The update algorithm is based on retrospective cost optimization.

subsystem, as shown in Figure 1, where the input signal \hat{y} and output signal \hat{u} of the unknown subsystem are not measured and thus cannot be used to estimate the unknown subsystem.

Alternatively, for the objective of estimating an unknown external input, RCAISE was used in [2] to estimate the unknown driver $F_{10.7}$ in a fully three-dimensional version of GITM using both simulated and real satellite measurements. In this case, as shown in Figure 2, the adaptive driver estimator is updated to obtain an estimate \hat{w} of the unknown driver w . These studies demonstrated that RCMR and RCAISE can effectively use data parameter, state, and input estimation within the context of a highly nonlinear, large-scale model consisting of thousands of state variables.

2.2 Estimation of the Eddy Diffusion Coefficient

In this section we briefly describe work where the goal is to estimate the eddy diffusion coefficient (EDC) of the thermosphere. The drag force felt by low-Earth orbiting objects is linearly proportional to the mass density of the thermosphere. Uncertainties in thermospheric mass density variations are the major limiting factor for precise low-Earth orbit determination. The perturbation of the thermospheric mass density is strongly controlled by the energy deposited into the upper atmosphere. The difference in the thermosphere mass density responses to different sources of energy input has been investigated, and the spatial and temporal variations of the thermospheric mass density during a series of idealized substorms were studied using the Global Ionosphere Thermosphere Model (GITM) [64]. The mass density response to different types of energy inputs was shown to have strong local time dependence. In addition, the thermosphere mass density response to different sources of energy input is a slightly nonlinearly system, and the non-linearity grows

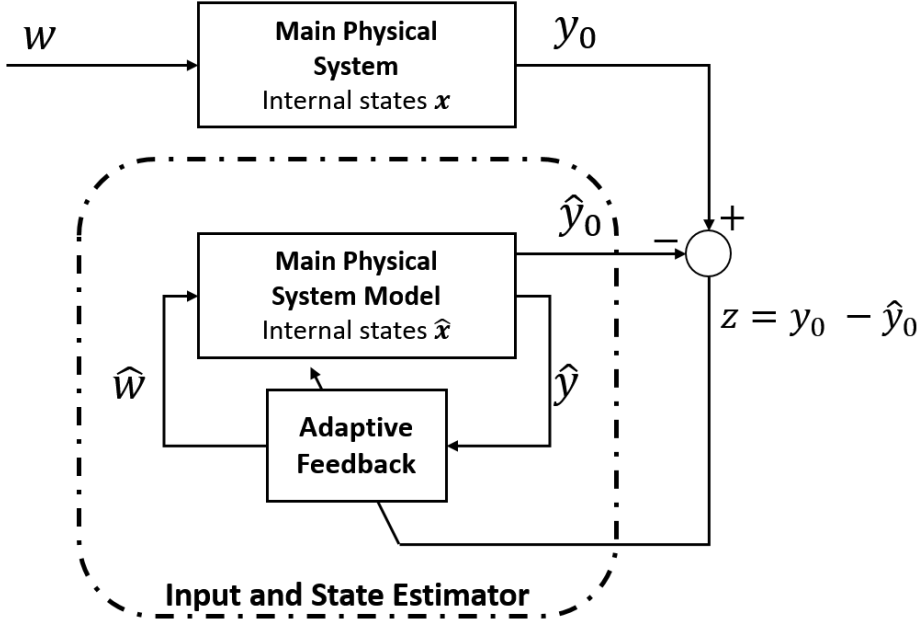


Figure 2: Retrospective Cost Adaptive Input and State Estimation (RCAISE) architecture. RCAISE uses the estimation error $z \triangleq y_0 - \hat{y}_0$ to adjust the adaptive driver estimator, which is used to construct an estimate \hat{w} of the unknown driver w . The update algorithm is based on retrospective cost optimization.

with the level of energy input.

The Eddy diffusion coefficient represents the mixing of the lower thermosphere composition. By controlling the thermo-conductions and the altitudes where the species begin to diffuse according to their particular scale height, variations in the Eddy diffusion coefficient strongly affect the upper thermosphere, and hence the ionosphere total electron content (TEC), which is a key parameter in the ionosphere. A goal of this work is to understand how EDC affects TEC. The effect of EDC variations on TEC was investigated in detail under various solar conditions, including the dependence of EDC on the F10.7 index.

The thermosphere composition change has a strong effect on the thermosphere mass density response, especially in the oxygen/helium transition region; however, most physical models do not include the effect of helium. To better represent the thermosphere mass density perturbations during geomagnetic storms, the helium component is implemented in the GITM model. In ongoing research, the morphology of helium simulated by the GITM model is being investigated and compared with measurement from the Atmosphere Explorer (AE) satellite.

The parameter EDC plays a key role in GITM and many CFD (computational fluid dynamics) codes. In particular, EDC in GITM models the turbulent mixing in the upper atmosphere. According to the mass continuity and the momentum equations, the altitude profile of the neutral constituents changes from fully mixing at lower altitudes, where turbulent mixing prevails, to molecular diffusion at higher altitudes (above 110 km). The value of EDC represents the intensity of the turbulent mixing, which is a key factor in controlling the upper atmosphere composition profiles.

In practice, it is challenging to estimate EDC from ground-based and satellite measurements [39, 58, 83], and efforts to estimate the value of EDC based on theoretical analysis have been made by [1, 41, 73]. Estimates of the EDC value based on measurements and/or theoretical modeling range from 25 to 1000

m^2/sec . In view of these diverse estimates, it is desirable to develop techniques that can estimate EDC based on the available data.

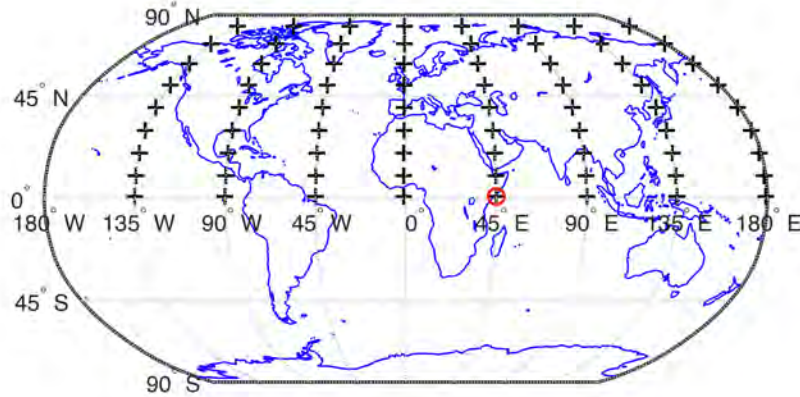


Figure 3: Simulated Ground Locations for Total Electron Count Measurements. Each "+" denotes the location of a simulated ground location for measurements of total electron count (TEC). Simulated data from these locations is used by RCMR to estimate the eddy diffusion coefficient in the thermosphere.

RCMR and RCAISE depend on modeling information about the system being considered; this modeling information can be viewed as a reduced-order model, or as tuning parameters, since often only a small number of parameters are needed. For a low-dimensional linear system, the required modeling information can be extracted in the form of the impulse response. For DDDAS applications, however, our interest is in high-dimensional nonlinear systems, such as the thermosphere as modeled by GITM, where the number of states may be as large as 10^7 . GITM is implemented by a FORTRAN code that captures diverse physics including fluid dynamics, thermodynamics, chemical kinetics, and electrodynamics. For this application, no analytical model is available, and it is not possible to analytically extract the required modeling information due to the complexity of the physics. Therefore, we typically implement RCMR and RCAISE using a small number of tuning parameters determined by numerical testing. As we have found in relation to the estimation of EDC using TEC measurements, this approach is inefficient.

What is needed to make RCMR/RCAISE a truly practical tool is a reliable, systematic, and easily implementable technique for obtaining the tuning parameters required by RCMR/RCAISE. One approach, which we have tested on low-order examples, involves iterative refinement of the tuning parameters that comprise the filter G_f . For a fixed data window, initial tuning parameters are chosen and used to obtain a subsystem model. This subsystem model is merged with main system model, and the resulting "closed-loop" impulse response is computed. The impulse response parameters are then used as tuning parameters within an updated filter G_f for re-estimating the unknown subsystem, and the process repeats using the same data window used in previous iterations. Tests have shown that this iterative filter refinement approach provides fast response from a possibly poor initial choice of G_f and is efficient in the sense that only limited data window is needed.

To illustrate this technique, consider a 2nd order linear system where A_{11} is uncertain. We assume that the nominal model of \hat{A} is such that $\hat{A}_{11} - A_{11} = \Delta A_{11} = 1$. We construct G_f from the impulse response of transfer function from \hat{u} to \hat{y}_0 . In subsequent iterations, G_f is refined using the updated value of \hat{A} . Figure

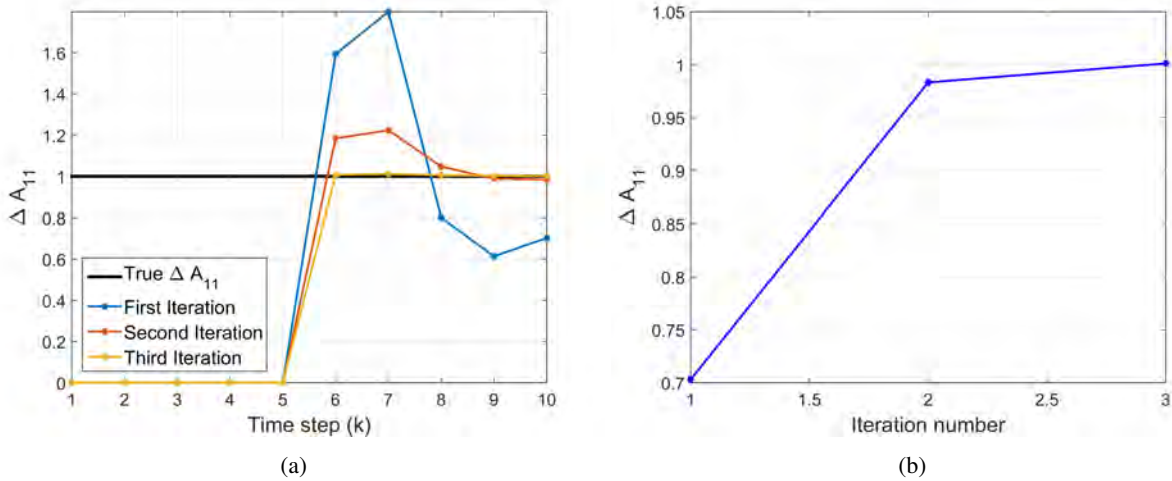


Figure 4: (a) RCMR estimate of ΔA_{11} with iterative filter refinement. The filter G_f is refined after each iteration based on the updated estimate of ΔA_{11} . Note that the data window for each iteration consists of only 10 time steps, RCMR is switched on after 5 time steps, and one-step estimation of the estimate of ΔA_{11} is achieved at the 3rd iteration. (b) Estimate of ΔA_{11} at the end of each iteration. After each iteration, G_f is refined using the updated estimate, and is used in the next iteration.

Figure 4(a) shows the estimate of ΔA_{11} in each iteration. Figure 4(b) shows the estimate of ΔA_{11} at the end of each iteration.

This G_f refinement technique has the added advantage that refinement of G_f is implemented on the same data set, and thus only a small amount of data is required to increase the rate of convergence. The final refined filter G_f is then used on the remaining data set. For nonlinear systems, this technique can simplify the numerical testing procedure for constructing G_f . If successful on large-scale applications such as GITM, this iterative filter refinement technique will significantly simplify the implementation of RCMR/RCAISE on new and challenging applications. In particular, this technique will facilitate the application of RCMR/RCAISE with greater assurance of success.

2.3 Cubesat Technology

An additional component of this project was the development of post-launch calibration techniques for spacecraft that collect data for atmospheric modeling. This effort ties into the development of Cubesats at the University of Michigan, several of which are currently in orbit [11, 22, 78]. New techniques were developed for calibrating on-board sensors after the spacecraft reaches its specified orbit. In particular, low-cost photoelectric and magnetic-field sensors typically lose calibration due to the launch and space environment. Through a combination of physics modeling and data analysis, it is shown in [89] that the accuracy of on-board sensors can be enhanced through ground-based re-calibration. This re-calibration accounts for time-varying electrical and magnetic fields, the Earth's spatially varying magnetic field, and sensor degradation.

Additional research has focused on design studies for spacecraft configurations. In particular, multidisciplinary design optimization techniques were applied in [51] to optimize multiple spacecraft subsystems, including power and communications subsystems. In addition, a study of photovoltaic power generation constraints due to spacecraft solar panel geometry, orbital effects, and self-induced shadowing is described in [61].

2.4 Scheduling for Satellite Data Downloading

The last component of this project addresses the challenges that arise from transferring data from a constellation of satellites. Data transfer is limited due to power and energy constraints, orbit trajectory, and the location, gain, and field of view of available ground-based stations. This leads to a capacity-constrained scheduling problem. These issues were addressed by developing real-time scheduling algorithms for modeling and optimizing space networks to optimize communication capacity [86, 88]. Research includes detailed investigations of download-scheduling techniques for configurations involving multiple satellites and ground stations [19, 62, 87].

2.5 Student Training

This project partially supported several students who received the Ph.D. degree, namely, Sara Spangelo, John Springmann, and Asad Ali, as well as postdoc Angeline Burrell. Continuing students include Ankit Goel in Aerospace Engineering as well as postdoc XianJing Liu. Brian Lemay and Jeremy Castaing are expected to complete their Ph.D. degrees in 2016 and 2017, respectively.

Two students supported by this project were recognized for their technical contributions. John Springmann was the winner of the Student Paper Competition at the AIAA 2013 Small Satellite Conference for [90]. Jeremy Castaing received honorable mention in the Student Paper Competition at the AIAA 2014 Small Satellite Conference for [19].

3 Background: Space-Weather Monitoring for Safety and Reliability

The near-Earth environment, in particular, the ionosphere-thermosphere, changes in response to solar phenomena. These phenomena include massive ejections of charged particles, which can disrupt the upper atmosphere and magnetic field of the Earth. These changes can have catastrophic effects of various types. First, changes in electrical properties affect the transmission of radio waves, which degrades the accuracy of GPS. Next, changes in density and wind speed affect the orbits of both operational satellites and debris. These orbital changes make it difficult to predict the possibility of collisions and take evasive action. Collisions have destructive consequences, and lead to more debris, which further exacerbates the problem. Finally, space weather can induce ground currents, which can destroy electrical transformers. The article [53] describes the potentially catastrophic consequences of such events, which have occurred several times during the last century and whose reoccurrence is thought to be inevitable.

The accuracy of predictions of satellite trajectories through the upper atmosphere depends on the accuracy of the drag model. The drag force F_d is modeled by $F_d = -\frac{1}{2}AC_d\rho\|V_s - V_w\|^2$, where A is the projected surface area of the satellite, C_d is the drag coefficient, ρ is the density, V_s is the velocity of the satellite, and V_w is the velocity of the upper atmospheric wind that the satellite encounters. In the upper atmosphere, the wind is typically 200-400 m/s, while the satellite orbital velocity is on the order of 7500 m/s; therefore, the wind is typically ignored. During strong upper atmospheric storms, however, the winds can increase beyond 1000 m/s. The density ρ is even more variable. For example, from night to day, ρ can increase by a factor of two. This means that as the satellite orbits (in 90 minutes), it traverses from the sunlit dayside to the colder nightside, encountering very different drag conditions. Furthermore, from solar minimum conditions, when the sun is dimmest in X-ray wavelengths, to solar maximum (5-6 years later), when it is brightest in those wavelengths, the nominal density can increase by more than an order of magnitude. Density can also increase dramatically on short time-scales; for example, during a storm ρ has significant localized structure and, globally averaged, can increase by a factor of two or three in just a few

hours (3-4 orbital periods). These types of storms cause the Joint Space Operations Center to miscalculate the trajectories of thousands of objects, and days of effort are needed to re-acquire their orbital positions.

Fig. 5 illustrates the variation in ρ observed by the CHAMP satellite [10] over four days, during which two large storms occurred. The upper plot shows 1-minute averaged data, while the lower plot shows data averaged over a 90-minute orbit. The maximum density observed by the satellite is roughly 28×10^{-12} kg/m³, while the smallest density is about 4×10^{-12} kg/m³, that is, a factor of seven smaller. The variability observed over the orbit in the upper plot is a result of the satellite passing through the warm summer dayside into the cold winter nightside. When the data are averaged over an orbit, increases during the storm times are apparent. The rises are very fast, and ρ approximately doubles over the course of a few hours.

Empirical models of the upper atmospheric density are used to predict orbital trajectories. Since these empirical models were found to lack the ability to accurately estimate ρ , the Department of Defense launched approximately 200 spheres, which simply orbit the Earth and are affected by the drag. Their position is determined by radar twice a day, so that the empirical models can be “corrected” by scaling to compensate for the global error. Although these empirical models are easy to run, they are crude and have limited accuracy.

The most proactive approach to dealing with the effects of space weather is to sense disturbances at the earliest possible stage and take evasive action. Long-term (up to three-day) prediction requires measurements of solar activity collected by spacecraft in solar orbit as well as spacecraft at the Lagrangian point that monitor the solar wind. These sensors provide advance knowledge of solar storms, which can then be used to predict the impact on the ionosphere-thermosphere. The project that we propose focuses on one component of the space weather problem, namely, monitoring of the ionosphere-thermosphere. As we describe below, this objective requires multiple transformative advances in DDDAS.

4 Relevance of DDDAS to Space Weather Monitoring

The long-term motivation for this DDDAS project is to develop a constellation of Cubesats that can provide data to dynamically monitor the ionosphere-thermosphere. A constellation of approximately 40 Cubesats in different orbits would provide the ability to monitor the atmosphere in a global 24/7 manner. Each Cubesat would be equipped with a suite of sensors for monitoring properties of the ionosphere-thermosphere. Data would be stored on-board and communicated to the ground where it could be used for modeling and prediction.

The operation of this constellation, however, requires multiple transformative advances in DDDAS. For starters, each Cubesat has limited energy and power, which constrains the ability of each Cubesat to send and receive data. The power needed for communication depends partially on the ground station, and ground stations vary widely in their ability to send and receive data as well as their availability, which can change from hour to hour. Further complicating the communication problem is the fact that each Cubesat is in a different orbit and has only partial information about the availability of ground stations along its path. At the same time, the ground controller has limited ability to communicate with each Cubesat to update it on ground-station availability.

While these issues suggest the dynamic nature of the problem of the data collection problem, the DDDAS nature of the problem becomes much more complex when the dynamics of the atmosphere are taken into account. Consider, for example, the following scenario. Each Cubesat has an on-board GPS system, and it also has some computational ability that it can use to predict its own location. When a Cubesat’s predicted location varies significantly from its measured position, it can infer the presence of perturbations to the atmospheric density. The Cubesat can then begin to collect data at higher resolution than normal and, at the

same time, must determine an efficient means for transmitting its data to a ground station. The transmitted data are ultimately collected centrally, where it can be used for data assimilation. The results of the data assimilation, which must be performed at nearly a real-time rate, can be used to determine whether the disruption to the ionosphere-thermosphere is significant. If so, additional Cubesats can be enlisted to begin data collection in an optimal configuration and at an enhanced rate, while the downlinking for each Cubesat must be scheduled “on the fly” based on priorities set by the data assimilation.

This is only one scenario demonstrating how sensing, scheduling, data assimilation, and analysis of the results must work together to monitor the ionosphere. The key point is that each component of this system is dynamic and data driven, and that data assimilation must interact with data collection and vice versa in real time. This application thus reflects the goals, challenges, and opportunities of the DDDAS paradigm.

DDDAS seeks transformative advances in four frontiers, namely, Applications Modeling, Mathematical and Statistical Algorithms, Application Measurement Systems and Methods, and Advances in Systems Software. Research in each frontier is motivated by the dynamic data-driven aspects of the Cubesat constellation, data assimilation, and space weather conditions, all of which are essential to the overarching goal of monitoring space weather in real time. To achieve the required advances in each frontier, the following sections describe relevant research in each area. Each section describes the motivation for DDDAS-related research within the context of space weather monitoring along with recent research advances.

5 DDDAS Frontier: Applications Modeling

5.1 Context and Motivation within DDDAS

The foundation for space weather monitoring is a first principles model of the upper atmosphere, namely, the Global Ionosphere-Thermosphere Model (GITM) [77], which provides the basis for data assimilation algorithms. GITM is a 3-dimensional spherical code that solves the Navier-Stokes equations for the thermosphere. These types of models work better than empirical (ad hoc “correction”) models because they capture the dynamics of the system instead of snapshots of steady-state solutions, which are what most empirical models provide. Furthermore, first principles models, such as GITM, model the winds that can influence the drag. In order to accurately predict ρ and V_w in the upper atmosphere, GITM considers the densities of N_2 and O_2 , which are the main constituents at 100 km altitude, and NO, which becomes more dominant in the upper atmosphere.

GITM is different from most models of the atmosphere in that it solves the full vertical momentum equation instead of assuming that the atmosphere is in hydrostatic equilibrium, where the pressure gradient is balanced by gravity. While this assumption is fine for the majority of the atmosphere, in the auroral zone, where significant energy is dumped into the thermosphere on short time-scales, vertical accelerations often occur. This heating causes strong vertical winds that can significantly lift the atmosphere [30].

The grid structure within GITM is fully parallel, using a block-based, two-dimensional domain decomposition in the horizontal coordinates [70, 71]. The number of latitude and longitude blocks can be specified at runtime, so the horizontal resolution can easily be modified. GITM has been run on up to 256 processors with a resolution as fine as 0.31° latitude by 2.5° longitude over the entire globe with 50 vertical levels, resulting in a vertical domain from 100 km to roughly 600 km. This flexibility will allow us to validate accuracy by running data assimilation and input reconstruction at various levels of resolution.

It is possible to “fly” satellites through GITM. By listing the times and locations of measurement points, GITM can track the path of a satellite, outputting simulated data at the specified times and positions. This feature simplifies implementation and validation of data assimilation and input estimation. Fig. 5 shows

GITM simulation results during the four days corresponding to the CHAMP data. These results were output every minute from the simulation at the CHAMP location for direct comparison with the satellite. This type of comparison allows us to see how the simulation is reproducing storms in the upper atmosphere.

Because drivers are important to the upper atmosphere, GITM can be driven by a wide variety of solar brightness models [45, 74, 95, 100] and measurements [20, 98, 99]; auroral specifications [40, 42, 69]; and high-latitude electric potential models [37, 43, 79, 97]. In addition, the assimilative mapping of ionospheric electrodynamics (AMIE) technique [13, 55, 56, 75, 76, 80] can be used to more accurately estimate the high-latitude aurora and electric potential.

5.2 Physics-Driven Adaptive Modeling (PDAM)

The thermosphere and ionosphere mark the true transition of the atmosphere to the space environment. The top of the thermosphere (the exosphere) is where the collision frequency of the neutral particles drops low enough that it becomes difficult to describe them as fluids. In the lower thermosphere, the neutrals are still dominated by dynamics, such as solar tidal forcing, but, as altitude increases, and the density of ions also increases, the neutrals becomes more strongly controlled by ion forcing. Also, the density of the gas becomes so low that the flow speeds can become quite large, reaching over 1000 m/s on occasion. This speed is comparable to the sound speed, so it is possible to get supersonic flows in the upper atmosphere. Furthermore, because the flows and sound speed can be so large, the dynamics of the upper atmosphere are truly global—waves propagate from one side of the Earth to the other in just a few hours. This means that models need to consider the global system and not just focus on regional dynamics.

Ions, because they are charged particles, are driven by electric fields, which are much stronger than forces such as gravity and the gradient in pressure. The electric forces are so strong that the ions quickly reach an equilibrium velocity that can have a significant amount of small-scale spatial structure [54]. The neutrals, on the other hand, have much more inertia and are slow to react, so the ions serve to transfer momentum and energy (through friction) to the neutrals [29, 57]. This transference often happens on small scales in regions of large electron densities and strong electric fields, that is, in the auroral zone [31]. The heating on small scales causes localized perturbations in the thermospheric (neutral) temperature and pressure, which increase winds and eventually causes a global disturbance [12]. Therefore, it is often important to be able to capture small-scale dynamics. The problem is that the global-scale phenomena need to be captured as well.

Further complicating the issue is the fundamental modeling of the aurora and how it deposits energy into the thermosphere and ionosphere. The aurora, in essence, is a beam of electrons that is shot into the thermosphere. Many researchers have simulated how the atmosphere reacts to this beam of energy, and parameterized how this phenomenon deposits energy into the system [34, 38]. However, there are aspects of this process that are often simplified and are not taken into account when simulating active time periods. For example, models of the auroral energy deposition typically use a static thermosphere that is not disturbed [84]. The composition is typically static in the models, so the aurora precipitates into the same atmosphere continually. What really happens, though, is that, as the electrons penetrate into the atmosphere, heat is deposited, preferentially lifting the heavier species (such as N₂ and O₂), which changes the collision frequency between the beam of electrons and the atmosphere [17, 91, 92]. This is normally not a large concern since the amount of energy deposited is not substantial enough to change the composition significantly, but during large auroral events, this feedback should be considered.

6 DDDAS Frontier: Mathematical and Statistical Algorithms

6.1 Context and Motivation within DDDAS

The ionosphere and thermosphere are strongly driven by the Sun. This means that the evolution of the thermosphere depends primarily on the input from the Sun rather than its current state. In other words, the effect of an initial state tends to be “washed away” by the input. Consequently, estimates of solar drivers can greatly enhance the accuracy of state estimates obtained from data assimilation with unknown inputs. Obtaining accurate estimates of these drivers represents an application and challenge to DDDAS concepts and technology.

In the case of the upper atmosphere, the extreme ultraviolet radiation produces photo-ionization, which in turn, through chemistry and heating, drives the properties of the ionosphere and thermosphere. Since a significant portion of the EUV and X-ray radiation is absorbed in the atmosphere, it is not possible to measure the flux from the ground. Instead, a proxy is used. The flux solar irradiance at a wavelength of 10.7 cm (called F10.7) is thus measured on the ground and used to estimate the solar spectrum in the 0-150 nm range. The unit of F10.7 is $10^{-22} \text{ W/Hz/m}^2$, which is equivalent to 1 solar flux unit.

Although good estimates of F10.7 can enhance data assimilation in the ionosphere-thermosphere, estimates of F10.7 are infrequent (for example, once per day) and approximate. This situation motivates the need to estimate F10.7 concurrently with the states. This is a problem of *input estimation*.

6.2 Retrospective Cost Adaptive Input and State Estimation (RCAISE) for DDDAS

State estimation techniques, such as the Kalman filter and its numerous variants, use measurements to recursively refine state estimates. In the simplest case, the system of interest has the form

$$x(k+1) = Ax(k) + Bu(k) + w(k), \quad (6.1)$$

$$y(k) = Cx(k) + v(k), \quad (6.2)$$

where $x(k)$ is the state and $y(k)$ is the available measurement. The input to the system is modeled as a combination of a known deterministic signal $u(k)$ and an unknown stochastic signal $w(k)$. The known deterministic signal $u(k)$ is injected numerically into the observer (not shown here), which uses knowledge of the statistics of $w(k)$ and the sensor noise $v(k)$ as well as knowledge of the matrices A and C to obtain an estimate $\hat{x}(k)$ of the state $x(k)$. This is how an estimator works. In practice, however, the deterministic input $u(k)$ is often unknown, or at least partially uncertain. A common practice is thus to treat $u(k)$ as part of the stochastic input $w(k)$. This approach, however, can yield poor state estimates for the simple reason that the characteristics of $u(k)$ may be quite different from the assumed statistics of $w(k)$.

Because of uncertainty in $u(k)$, extensive research has been devoted to developing extensions of the Kalman filter that are either insensitive to knowledge of the deterministic input or that attempt to estimate this signal in addition to the states. These techniques are referred to as unbiased Kalman filters, unknown input observers, input estimators, and state estimators with input reconstruction. The literature is extensive [14, 36, 49, 59, 60, 72, 94, 96, 101], but no unified techniques have yet emerged, and application to large-scale data assimilation has been limited.

The importance of input estimation is due to the fact that, for many systems, the effect of the initial state decays, and thus the asymptotic response is governed entirely by the forcing. In the linear case, systems with this property are asymptotically stable. In the nonlinear case, these systems are called *incrementally stable* or *contractive*, and the relevant phenomenon is called *entrainment* [9, 81, 85]. The presence of entrainment suggests that, at least in some cases, the accuracy of state estimation can be greatly enhanced by the ability

to perform input estimation. The goal of this research on data assimilation is thus to reconstruct the inputs to the system concurrently with the estimates of the state. If the inputs can be estimated recursively, then the accuracy of the input reconstruction can be significantly enhanced in comparison with state estimation alone.

In support of the DDDAS Frontier Mathematical and Statistical Algorithms, this task is

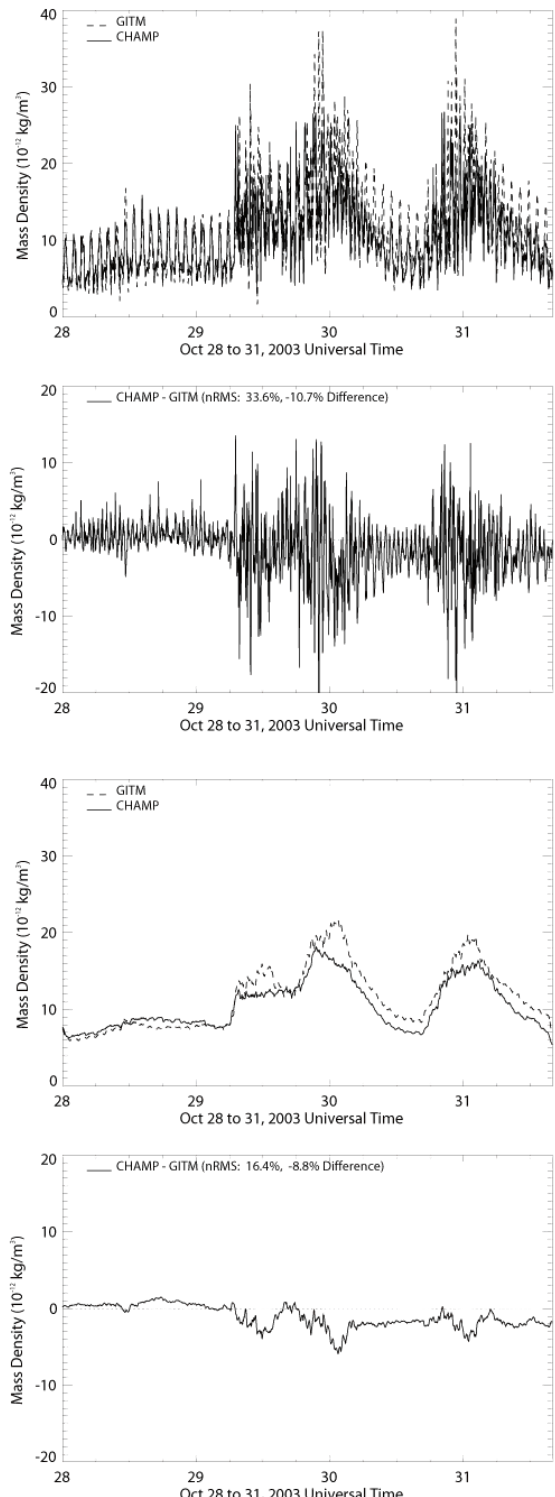


Figure 5: The atmospheric density ρ at 407 km altitude measured by the CHAMP satellite (solid line) along with simulation results from GITM (dashed line). The upper plot show one-minute values of the results, while the lower plot shows orbit-averaged (i.e., 90-minute) values focusing on the development and application of Retrospective Cost Adaptive Input and State Estima-

tion (RCAISE) [26]. The RCAISE architecture is shown in Figure 6, where the error $z(k)$ represents the difference between measured and estimated quantities in the ionosphere-thermosphere. RCAISE is an outgrowth of research we have performed on adaptive control and model refinement using the retrospective optimization technique described in [25, 28, 46–48, 65, 82, 93].

Within the context of data assimilation for large-scale applications, input estimation can be performed by applying ensemble Kalman filter techniques [3–7, 16, 52, 63]. These techniques employ an ensemble of simulations, which can be chosen to include a distribution of representative values of the unknown input. The computational burden of this approach thus increases in relation to the number of ensemble members. Unlike ensemble filtering, however, RCAISE uses a single simulation model as the basis of both state estimation and input reconstruction. Consequently, unlike particle filters, RCAISE is an *ensemble-free technique for data assimilation with input reconstruction*. The price paid for this convenience, however, is the lack of an error distribution on the estimated input.

The prior literature on state estimation with input estimation [14, 36, 49, 60, 72, 94, 96, 101] provides alternative techniques for this problem. However, these techniques are largely confined to linear systems, whereas DDDAS applications, such as space weather monitoring, are typically highly nonlinear. For systems with nonlinear dynamics, RCAISE does not rely on an analytical model of the system, requiring only the ability to update the simulation of the system, and this simulation can be in the form of a large-scale computer code, such as GITM.

6.3 Earlier Research Results

We now summarize recent results describing the application of RCAISE to the ionosphere-thermosphere. An overview is given in [24]. The objective of input estimation supports the goals of DDDAS by enhancing prediction accuracy. In particular, state and input estimation are considered in [2] based on the 3D GITM model with both synthetic and real measurements. Here we consider the case of real measurements from the CHAMP satellite.

This study is motivated by the fact that radio propagation and satellite drag are affected by the Sun's influence on the ionosphere and thermosphere. In particular, extreme ultraviolet (EUV) and X-ray radiation produce photo-ionization, which, in turn, through chemistry and heating, drives the formation of the ionosphere and shapes the thermosphere. In addition, the effect of the EUV and X-ray radiation is sufficient to render the ionosphere-thermosphere a strongly driven system [9, 81, 85].

Since a significant portion of EUV and X-ray radiation is absorbed by the atmosphere, it is not possible to measure these quantities from the ground. Instead, a proxy is used. The most common proxy for EUV and X-ray radiation is the flux solar irradiance at a wavelength of 10.7 cm ($F_{10.7}$), which is measured (in

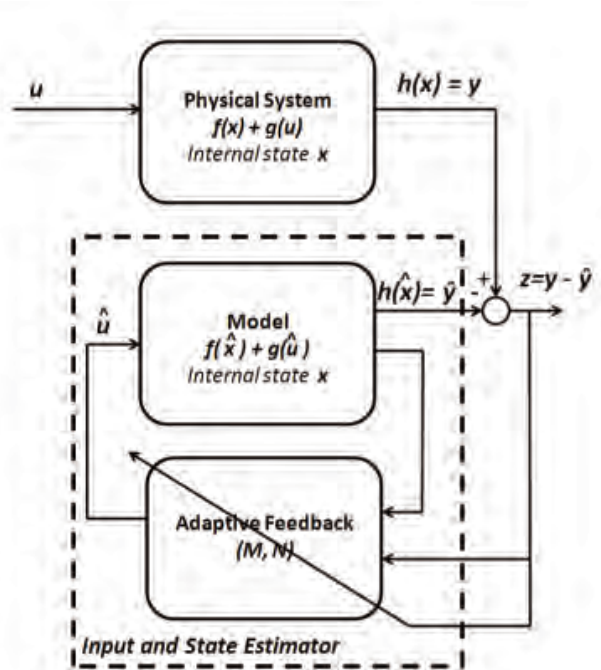


Figure 6: State and input estimation architecture. Based on the estimation error $z = y - \hat{y}$, the adaptive algorithm adjusts the the feedback block, which estimates the unknown input u .

units of $10^{-22} \text{ W Hz}^{-1} \text{ m}^{-2} = 1$ solar flux unit (SFU)) by the Dominion radio observatory in Penticton, Canada [68]. A shortcoming of this technique is that $F_{10.7}$ does not have a one-to-one correlation with each of the wavelengths in the EUV and X-ray bands, and thus the measured $F_{10.7}$ is often a misrepresentation of the true solar spectrum.

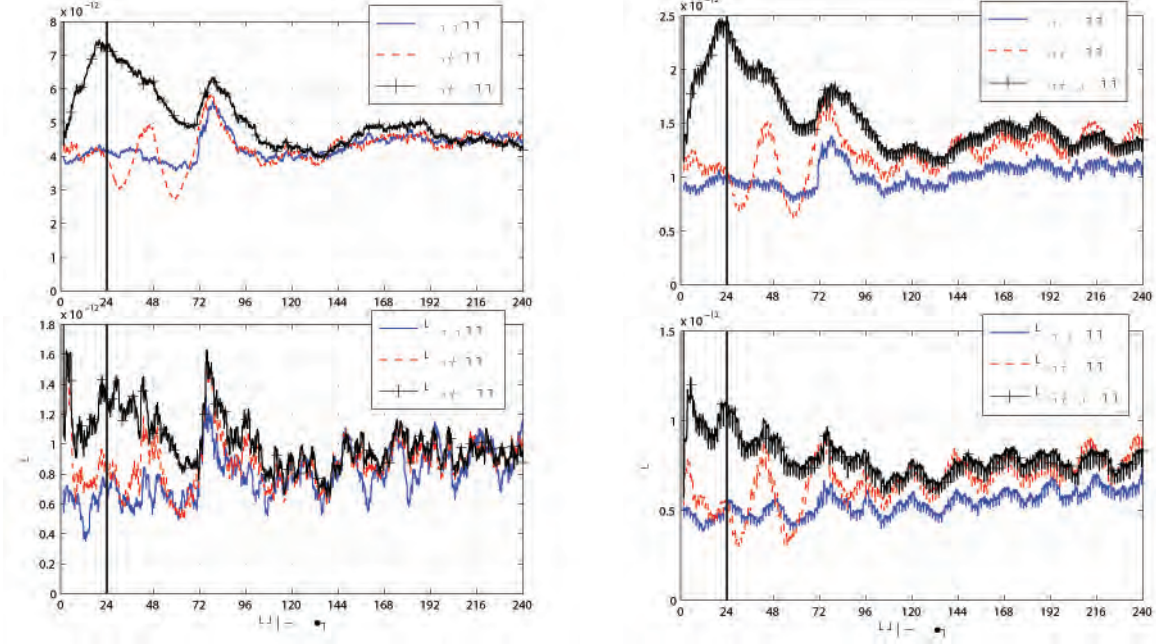
Although our ultimate goal is to estimate the true flux in multiple EUV and X-ray wavelength bins, a more attainable intermediate goal is to estimate the value of $F_{10.7}$ that best characterizes the ionosphere and thermosphere. The ability to estimate $F_{10.7}$ from alternative measurements can provide a cross check on the available measurements, while also providing an illustrative proof-of-concept demonstration of RCAISE as a first step toward estimating X-ray and EUV in multiple bands. Furthermore, current models do not fully capture the dynamics of the ionosphere-thermosphere, in which case $F_{10.7}$ can be used as an input to the model in order to eliminate the errors between real measurements and synthetic (simulated) measurements. This study thus attempts to specify $F_{10.7}$ based on simulated measurements of the atmosphere as well as with real satellite data. The specified $F_{10.7}$ can then be used to obtain improved estimates of the state of the ionosphere and thermosphere globally and possibly predict its future evolution. This is a problem of state and input estimation.

To estimate $F_{10.7}$, we use the Global Ionosphere Thermosphere Model (GITM) [77]. GITM simulates the density, temperature, and winds in the thermosphere and ionosphere across the globe from 100 km to 600 km altitude, depending on the solar conditions at the time. The main inputs to GITM are the high-latitude electrodynamics (i.e., the aurora and the associated electric fields), tides from the lower atmosphere, and the brightness of the sun at various wavelengths, which can be proxied through the use of $F_{10.7}$. GITM solves for the chemistry, dynamics, and thermodynamics of the upper atmosphere self-consistently by accounting for interactions among various species of ions and neutrals.

In [2] we used the retrospective cost adaptive state estimation (RCAISE) technique [27] to estimate the unknown solar driver $F_{10.7}$ using the Global Ionosphere-Thermosphere Model and satellite measurements. RCAISE assumes that the input to the system is unknown, and uses retrospective optimization to construct an input to the adaptive estimator that minimizes the retrospective cost function. The retrospectively optimized input is then used to asymptotically drive the error between the measured output and the estimator output to zero. In this way, RCAISE asymptotically estimates the unknown input to the system and the unknown states of the system. A useful feature of RCAISE is that an explicit nonlinear or linearized model is not required. In addition, unlike ensemble-based data-assimilation algorithms [8, 33, 50], RCAISE uses only one copy of the system model and thus is ensemble-free.

For the case of real satellite data case, the neutral mass density data measured by CHAMP (the “truth data”) is labeled $y(k)$, while the neutral mass density data measured by GRACE is labeled $y_G(k)$. First, we run GITM with the measured $\bar{F}_{10.7}(k)$ and record the neutral mass density at CHAMP locations and GRACE locations, which are labeled $\hat{y}_m(k)$ and $\hat{y}_{G,m}(k)$, respectively. Next, we combine RCAISE and GITM, and use $y(k)$ to estimate $\bar{F}_{10.7}(k)$ and states. The neutral mass density output from GITM with RCAISE at CHAMP and GRACE locations are labeled $\hat{y}(k)$ and $\hat{y}_G(k)$, respectively. Note that data from GRACE are used only as a metric for assessing the accuracy of state estimates, and are not used by RCAISE. We further divide this setup into two cases. First, in RCAISE, we use GITM with photoelectron heating. When photoelectron heating is used in GITM, then the neutral density output from GITM at CHAMP locations using measured $\bar{F}_{10.7}(k)$ closely matches CHAMP neutral density measurements. However, it should be noted that the photoelectron heating efficiency coefficient that yields low error between GITM and CHAMP is obtained by trial and error, and cannot be calculated or measured. In the second case, in RCAISE, we use GITM without photoelectron heating. In this case, GITM with measured $\bar{F}_{10.7}(k)$ yields a large error between the outputs from GITM at CHAMP locations and CHAMP measurements. In this case, RCAISE will use $\hat{\bar{F}}_{10.7}(k)$ as an input to GITM in order to correct the errors between CHAMP measurements and

the output from GITM at CHAMP locations, and thus account for the inaccuracies incurred by removing photoelectron heating from GITM.



(a) Output-matching performance of RCAISE for GITM using driver estimates.

(b) State-estimation performance of RCAISE for GITM.

Figure 7: (a) $\mu_{90,y}(k)$, $\mu_{90,\hat{y}_m}(k)$, $\sigma_{90,y}(k)$, $\sigma_{90,\hat{y}_m}(k)$, and $\sigma_{90,\hat{y}_m}(k)$ for the case of real CHAMP satellite data and GITM with photoelectron heating. For this example, GITM with RCAISE yields 6% lower $\text{RMS}(z)$ compared to GITM with measured $\bar{F}_{10.7}(k)$. (b) This plot shows $\mu_{90,y_G}(k)$, $\mu_{90,\hat{y}_G}(k)$, $\mu_{90,\hat{y}_{G,m}}(k)$, $\sigma_{90,y_G}(k)$, $\sigma_{90,\hat{y}_G}(k)$, and $\sigma_{90,\hat{y}_{G,m}}(k)$ for real GRACE satellite data and the case of real CHAMP satellite data and GITM with photoelectron heating. For this example, GITM with RCAISE yields 11% reduction in $\text{RMS}(z_G)$ compared to GITM with measured $\bar{F}_{10.7}(k)$.

Let $p(k) \in \mathbb{R}$ be an arbitrary signal, and let T be a positive integer. Then, for all $k \geq T$, define the windowed average of the signal $p(k)$ as

$$\mu_{T,p}(k) \triangleq \frac{1}{T} \sum_{i=k-T+1}^k p(i),$$

where T is the interval over which the signal is averaged. Similarly, for all $k \geq T$, define the windowed standard deviation of the signal $p(k)$ as

$$\sigma_{T,p}(k) \triangleq \sqrt{\frac{1}{T} \sum_{i=k-T+1}^k (p(i) - \mu_{T,p}(i))^2}.$$

The root mean square value of $p(k)$ is denoted by $\text{RMS}(p)$.

When GITM is used with RCAISE, we keep $\hat{F}_{10.7}(k)$ at a constant value of 100 SFU for the first 24 h, after which RCAISE is turned on. This allows the response due to initial conditions to decay significantly. We implement GITM on four processors with a resolution of 5° latitude by 5° longitude. The time step for

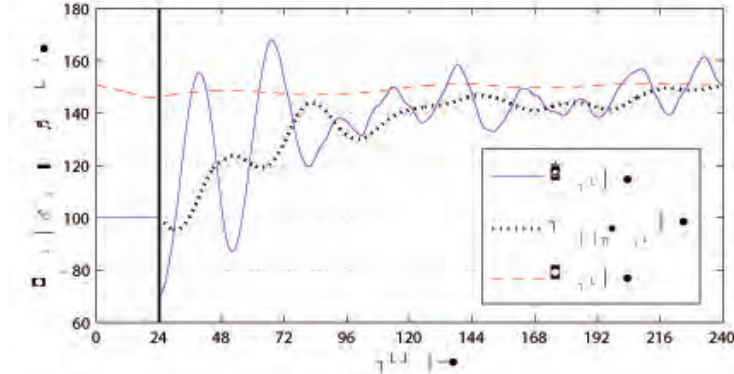


Figure 8: Measured and estimated $\bar{F}_{10.7}(k)$ for the case of real CHAMP satellite data and GITM with photoelectron heating. This plot shows that $\mu_{1440, \hat{F}_{10.7}}(k)$ (the average of $\hat{F}_{10.7}(k)$ over 1 day) converges to within 6 SFU (solar flux units) of the measured values of $\bar{F}_{10.7}(k)$ in 72 h.

GITM is set at 2 sec, and RCAISE is used to update $\hat{F}_{10.7}(k)$ every 60 sec. In all figures in this section, the vertical black line indicates when RCAISE is switched on. Finally, the numerical experiments consider the period from 2002-11-24 to 2002-12-06.

We consider the case where the truth data are recorded by CHAMP from 2002-11-24 to 2002-12-06 and we use GITM with photoelectron heating. We calculate the RMS of $z(k)$ after 144 h in order to minimize the effect of transients in $\hat{y}(k)$ generated during the convergence of the adaptive subsystem. First, we consider the measurements from CHAMP. Figure 7(a) shows the windowed mean and variance of $y(k)$, $\hat{y}(k)$, and $\hat{y}_m(k)$. For this example, GITM with measured $\bar{F}_{10.7}(k)$ yields $\text{RMS}(z) = 6.5 \times 10^{-13}$, and GITM with RCAISE yields $\text{RMS}(z) = 6.1 \times 10^{-13}$. In other words, GITM with RCAISE yields 6% reduction in $\text{RMS}(z)$ compared to GITM with measured $\bar{F}_{10.7}(k)$.

Figure 8 shows the measured and estimated $\bar{F}_{10.7}(k)$. This plot shows that $\mu_{1440, \hat{F}_{10.7}}(k)$ (the average of $\hat{F}_{10.7}(k)$ over 1 day) converges to within 6 SFU of the measured values of $\bar{F}_{10.7}(k)$ in 72 h.

Finally, we consider data from GRACE to assess the quality of the state estimates. Define $z_G(k) \triangleq y_G(k) - \hat{y}_G(k)$. Figure 7(b) shows the windowed mean and variance of $y_G(k)$, $\hat{y}_G(k)$, and $\hat{y}_{G,m}(k)$. For this example, GITM with measured $\bar{F}_{10.7}(k)$ yields $\text{RMS}(z_G) = 4 \times 10^{-13}$, whereas GITM with RCAISE yields $\text{RMS}(z_G) = 3.6 \times 10^{-13}$. Therefore, GITM with RCAISE yields 11% reduction in $\text{RMS}(z_G)$ compared to GITM with measured $\bar{F}_{10.7}(k)$.

7 DDDAS Frontier: Application Measurement Systems and Methods

7.1 Context and Motivation within DDDAS

The in-situ measurements required for GITM are difficult to make. First, they must be made in space, that is, in the ionosphere and thermosphere. Space is a harsh environment where extreme thermal fluctuations, high vacuum levels, and high-energy radiation require specialized, hardened electronics and systems. These specialized space-based sensors are expensive to build. Also, launches are infrequent and expensive. Second, these measurements are multiscale in time and space. At orbital velocities (~ 8 km/s), steep gradients in the thermosphere approach rapidly and require fast sampling. Our measurement environment is on a global scale, covering more than 577 million square kilometers. This is beyond current sensing and space system capabilities.

A potentially desirable feature of the system under study, the thermosphere, is the event-driven nature of the system; solar storms drive thermospheric changes. Storm-time dynamics are the least understood and, consistent with the goals and vision of DDDAS, that is precisely when high resolution data is most valuable to the data assimilation software. Thus, a collaboration between the applications modeling (GITM) and the system operating and tasking the satellites is needed to task the sensing systems (satellites) in real time in order to adjust sensing capabilities while accounting for physical constraints on the satellites such as power availability. In space systems, the science team and the satellite operations team are often not tightly coupled, residing in separate locations, and communication between them is slow. It can take days to weeks to re-task the satellite for new, advanced operational modes. Thus, our effort to enable real-time tasking of the satellites by the modeling system represents a novel and highly nontrivial advance in capability.

The foundation for our space weather monitoring effort is a low-cost satellite constellation composed of Cubesats, an industry standard satellite form factor that has a space-qualified launch vehicle interface, the P-Pod [15, 67]. More than fifty Cubesats have flown on rockets from the US, Europe, and Asia, and are being built by institutions ranging from universities to Government space programs (NASA) to established aerospace corporations such as Lockheed Martin and Boeing. At the University of Michigan, we have developed and launched several Cubesat missions for space weather research and technology demonstration. Developed for the National Science Foundation, two satellites for the Radio Aurora Explorer (RAX) mission were launched in 2010 and 2011, respectively, to study plasma instabilities that lead to magnetic field-aligned irregularities of electron density in the lower polar thermosphere (80–300 km) [11]. RAX-2 is currently fully operational and supporting bistatic radar experiments with transmitters located in Alaska and Canada. We are also developing CADRE, the Cubesat-investigating Atmospheric Density Response to Extreme driving, to make measurements specifically for thermospheric modeling and data assimilation. CADRE will be ready for launch in late 2013 [22, 78].

GITM requires neutral densities of the main constituents of the thermosphere, in particular, the neutral winds, the ion densities of the main ions, and the ion flows. Instruments are available for obtaining these measurements. The Ionospheric Miniaturized Electrostatic Analyzer (iMESA) provides electron density and temperature measurements using a miniaturized electrostatic spectrum analyzer [32]. The Gated Electrostatic Mass Spectrometer (GEMS) is based on an electrostatic energy analyzer and provides thermospheric composition data [44]. These sensors are compatible with the Cubesat form factor [35].

We thus have a challenging, multiscale sensing requirement from our advanced model system that is not possible with current technology. The foundation for this sensing system is a constellation of approximately 40 low-cost Cubesat-based sensors. Cubesats are extremely inexpensive compared to traditional, monolithic satellites and thus provide an enabling technology for distributed sensor networks in space. However, fundamentally new capabilities are needed to enable this system.

7.2 Research Effort: Event-Based Sensor Reconfiguration (EBSR)

Within the DDDAS Frontier Application Measurement Systems and Methods, we are developing a new capability to support space-based, multiscale measurements, namely, *event-based sensor reconfiguration* (EBSR). We consider sensing platforms and support systems that are reconfigurable. For example, dynamic elements could include data-collections rates, sensor selection, sensor physical distribution, and sensor directionality. Consistent with DDDAS, sensor reconfiguration is most advantageously based on events, both physical from the environment and feedback-based from the data assimilation and operations system. This will enable closed-loop, real-time sensor-system modification consistent with DDDAS goals and vision. Although motivated by the space-based domain, the fundamental characteristics of EBSR can be summarized in terms of three primary elements: 1) the system must be able to reconfigure; 2) the system must be able to determine when to reconfigure; and 3) the system must collect relevant telemetry and data to inform the

determination system.

Our work this past year emphasized *in-field sensor calibration*, which addresses elements 1) and 3). Calibration is the development of a transfer function that maps sensor readings to actual (that is, physical) values as well as a quantification of the errors in the sensor measurements. By definition, reconfiguration changes systems properties, and this typically requires sensor recalibration. Thus, by performing in-field calibration, we can extend our capabilities for reconfiguration.

7.2.1 Magnetometer Calibration

We finalized our method for in-field, attitude-independent magnetometer calibration, which includes the effect of time-varying bias due to electronics on-board a vehicle. The calibration estimates magnetometer scale factors, non-orthogonality, and both constant and time-varying bias. The unique contribution of this effort is the estimation of time-varying magnetometer bias due to nearby electronics. It is accomplished by including vehicle telemetry in the measurement model and estimating constant parameters that map time-varying currents to magnetometer bias. Calibration was demonstrated based on flight data from the RAX-1 satellite, and was shown to significantly reduce the uncertainty of off-the-shelf magnetometers embedded within the satellite and subject to spacecraft-generated fields. This method simplifies the satellite design process by reducing the need for booms and expensive magnetic cleanliness, resulting in reduced satellite development time and cost. In addition to on-orbit magnetometers, the calibration method is applicable to air, ground, and water navigation.

The developed model is given by

$$\tilde{B}_x = aB_x + x_0 + \sum_{i=1}^r s_{i,\tilde{x}} \tilde{I}_i + \eta_x, \quad (7.1)$$

$$\tilde{B}_y = b[B_y \cos(\rho) + B_x \sin(\rho)] + y_0 + \sum_{i=1}^r s_{i,\tilde{y}} \tilde{I}_i + \eta_y, \quad (7.2)$$

$$\tilde{B}_z = c[B_x \sin(\lambda) + B_y \sin(\phi) \cos(\lambda) + B_z \cos(\phi) \cos(\lambda)] + z_0 + \sum_{i=1}^r s_{i,\tilde{z}} \tilde{I}_i + \eta_z. \quad (7.3)$$

The recalibration procedure estimates magnetometer scale factors, non-orthogonality, and constant as well as time-varying bias. The time-varying bias is captured in the term, $\sum_{i=1}^r s_{i,j} \tilde{I}_i$, $j \in \{\tilde{x}, \tilde{y}, \tilde{z}\}$, where $s_{i,j}$ is the coefficient that maps the i -th current measurement \tilde{I}_i to the magnetic field in the j -th magnetometer axis, and r is the number of current measurements included in the model. Although current measurements are required for re-calibration, on-board current sensors are typically part of spacecraft health monitoring. Hence inclusion of the current measurements in the recalibration does not require additional sensors for the purpose of recalibration. Most importantly, this model does not

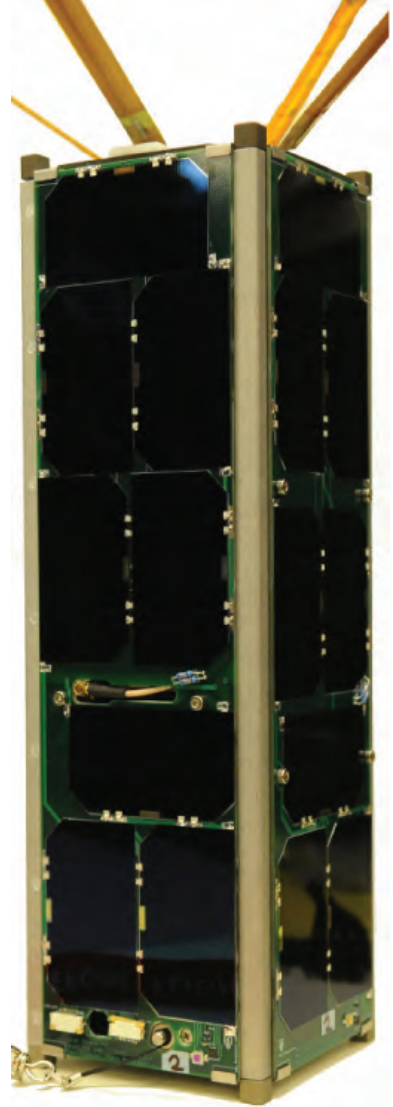


Figure 9: The Radio Aurora Explorer (RAX) triple Cubesat developed at the University of Michigan.

require any knowledge about the layout of the electronic components; the recalibration requires only current measurements, magnetometer measurements, and the expected magnitude of the geomagnetic field.

The calibration model was applied to data from the RAX-1 satellite [23]. From the data presented in Figure 7.2.1, we found that currents produced by the solar panels degrade the magnetometer measurements. There are four body-mounted solar panels on RAX-1, and we include measurements of the current in each panel. From further experimentation with the on-orbit data, we have seen that a fifth element, the current drawn from the battery, degrades the measurements [89]. Therefore, we include these five current measurements in the magnetometer model.

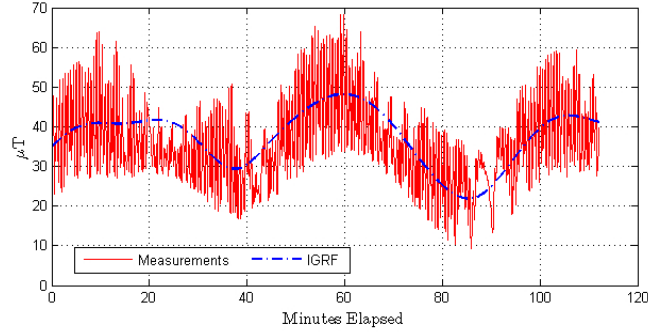
The results of the calibration are shown in Figure 11. Figure 11(a) shows the magnitude of the corrected measurements overlaid with the expected field magnitude, Figure 11(b) shows the difference between the measured and expected magnitudes, and Figure 11(c) is a histogram of the difference. Figures 11(a) and 11(b) show the significant improvement of the magnetometer data compared to the corresponding time-invariant calibration results shown in Figures 10(b) and 10(c). The root mean squared error (RMSE) of the measurements after calibration for time-invariant errors is 903 nT, where error is defined as the difference between the expected magnitude and the magnitude of the corrected measurements. After calibration with time-varying bias, the RMSE is reduced to 174 nT, an improvement factor of 5.2. This factor corresponds to an order of magnitude improvement in angular accuracy.

The resolution of the raw magnetometer measurements is 128 nT along each axis. The resolution of the corrected sensor readings in the orthogonal frame is transformed by the scale factors and non-orthogonality angles. After transformation of the 128 nT resolution with the calibration parameters, the resolution of the calibrated sensor is 144, 143, and 111 nT along the x, y, and z axes, respectively. This results in a 231 nT resolution on the magnitude of the corrected measurements. The RMSE of the calibrated data is only 174 nT, which is below the sensor resolution of 221 nT and indicates that the accuracy of the calibrated measurements has approached the precision limit of the sensor.

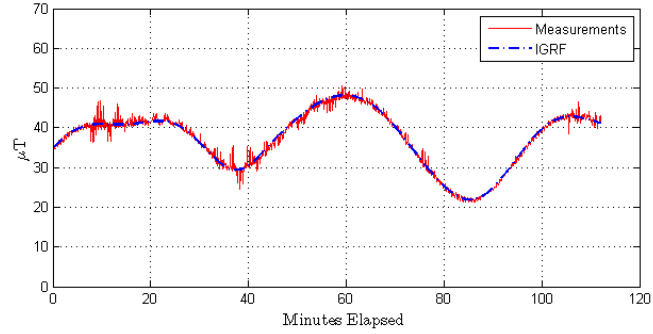
We have developed a method for on-orbit, attitude-independent magnetometer calibration that includes time-varying bias due to nearby electronics. Existing time-invariant calibration methods have been extended by including current measurements in the sensor model, and the resulting calibration method estimates both time-invariant errors and time-varying bias due to on-board electronics. The time-varying bias is estimated by mapping current to magnetometer bias through constant parameters. The calibration parameters are estimated using an iterative least-squares minimization, and only the magnetometer measurements, current measurements, and the expected magnitude of the geomagnetic field are required for the calibration.

The usefulness of the calibration has been demonstrated by application to on-orbit data. In application to the RAX-1 satellite, the calibration successfully mitigates magnetometer bias due to the satellite power system. The calibration improved the RMSE of magnetometer measurements from 792 nT to 219 nT, providing an order of magnitude improvement in angular attitude accuracy.

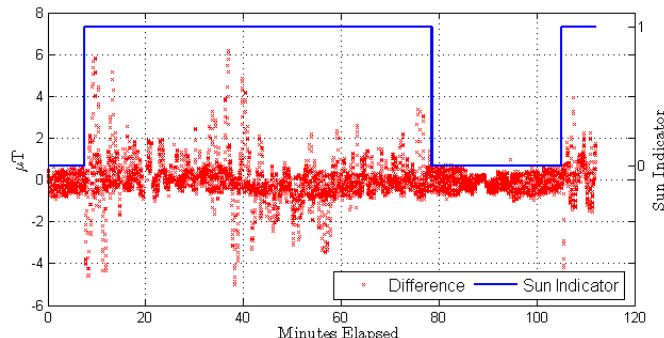
Traditionally, time-varying bias is mitigated by either using a boom to physically separate the magnetometer from the spacecraft, or by using design and manufacturing practices to minimize the influence of electronic components on magnetometers. Such design practices increase design time and cost, and physical separation of a magnetometer from on-board electronics may not be possible as satellites continue to decrease in size. The algorithm presented in this work effectively replaces such design practices with improved processing of the sensor measurements. The algorithm utilizes current sensors throughout the spacecraft, which are sampled at the same time as the magnetometers. Therefore, inclusion of current sensors and the ability to sample the sensors simultaneously for the purpose of calibration should be considered in the design phase of the vehicle. Although the calibration is a batch method, parameters can be uploaded to the spacecraft for real-time magnetometer correction, and real-time implementation will be developed in future work. The calibration has been applied to satellite-based magnetometers in this work, but this algorithm is



(a) Magnitude of the raw, uncalibrated measurements (μT) overlaid with the expected field magnitude using the IGRF model.

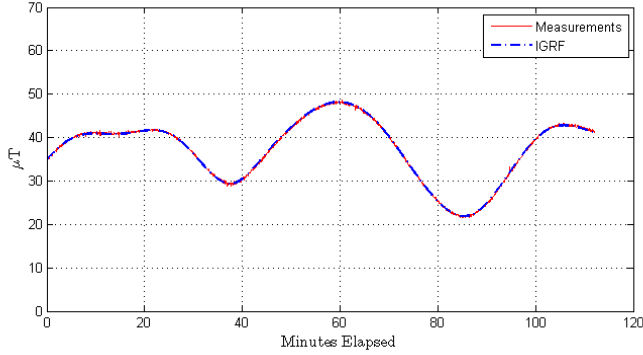


(b) Magnitude of the measurements after correcting for time-invariant errors (μT). The differences between the measured and IGRF magnitudes are shown in Figure 7.2.1.

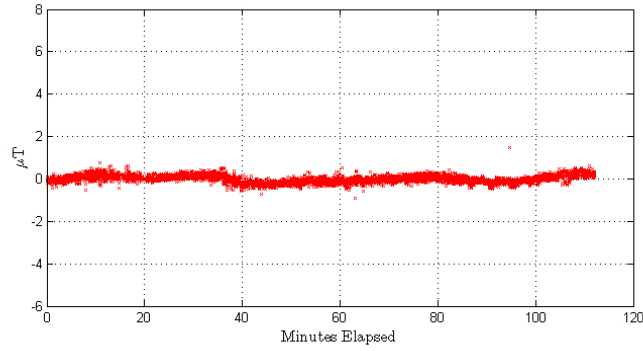


(c) The difference (μT) versus time. The sun indicator takes the value of one when RAX-1 is in the sun, and zero when in eclipse, which shows when the solar panels are illuminated and generating current.

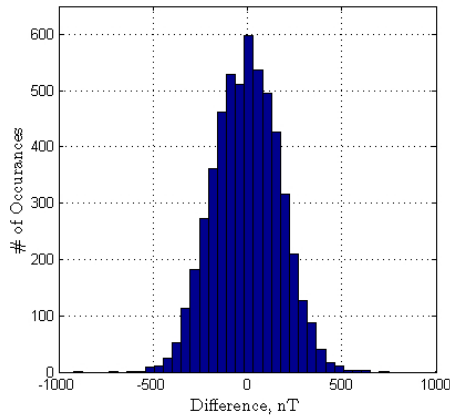
Figure 10: Data from the RAX-1 PNI MicroMag3 magnetometer. The x -axis of each plot shows time elapsed since the start of the data set, 01-Dec-2010 08:30:46 UTC.



(a) The magnitude of the corrected measurements (μT) versus time (minutes).
The magnitude of the expected magnetic field is overlaid.



(b) Difference between the corrected measured field magnitude and the expected magnitude (μT)



(c) Histogram of the difference between the measured and expected magnitudes (nT). There are 5,405 total data points.

Figure 11: Results of the calibration to estimate both constant errors and time-varying magnetometer bias.

applicable to other magnetometer applications on a variety of platforms.

7.2.2 On-Orbit Calibration of Photodiodes for Attitude Determination

We developed a method for on-orbit calibration of photodiodes for sun sensing in an attitude determination system [90]. The calibration estimates the scale factors and alignment angles of the photodiodes, resulting in higher attitude determination accuracy than achieved with the pre-flight calibration parameters. The calibration is implemented with an extended Kalman filter to simultaneously estimate spacecraft attitude and the calibration parameters. This approach, as opposed to an attitude-independent method, enables the calibration of an arbitrary number of photodiodes mounted in any orientation on the spacecraft and facilitates the use of an attitude-dependent Earth albedo model. The method is demonstrated by application to flight data from the RAX-2 satellite and results in an average angular improvement of 10° in sun vector measurements with the photodiodes. Attitude determination accuracies of below 1° in each axis are demonstrated using the calibrated photodiodes in combination with a low-cost three-axis magnetometer and rate gyroscope.

8 DDDAS Frontier: Advances in Systems Software

8.1 Context and Motivation

Previously, we discussed the need for new methods for collecting, analyzing, and using data gathered from the ionosphere-thermosphere to monitor space weather and thus better predict the orbital motion of large space objects. To successfully meet the goals outlined in these three sections, we also need to develop new models for scheduling and communicating policies on how to transmit these data to Earth.

Although we have posed (and will continue to discuss) this problem in the context of Cubesat data collection, the results that we are developing have much broader applicability. Specifically, we consider problems in which we have multiple clients (e.g., Cubesats) and multiple servers (e.g., ground stations). The clients are largely controlled by a central manager who provides policies to guide behavior; the clients in turn make local decisions based on these policies as well as on environmental factors that they experience (for example, a Cubesat might gather more data than originally planned if significant variation between its expected and observed location were detected). The central manager has discrete and possibly infrequent opportunities to communicate with the clients to update the policies. Finally, the clients are dependent on the servers, which themselves may be controlled by external agents, may have conflicts with other users, and may be subject to uncertainty in their availability and their performance characteristics. Problems of this type can be found in computing systems, telecommunication systems, energy systems, UAV systems, and many more real-world contexts. To address these fundamental, challenging, and widely applicable scheduling problems, we are developing heuristics, optimization-based algorithms, and simulation tools for hierarchical closed-loop scheduling (HCLS). Our work towards these goals is described below.

8.2 Modeling Space Communication Networks

We have developed a general, analytical framework for modeling an operational satellite mission. We define a framework as a set of reusable elements and templates for describing dynamics, constraints, and goals. The framework analytically represents the dynamic interaction of states (such as position, energy, and data) and subsystem operations (such as communication and energy management) of an operational satellite. It captures mission constraints, which are often called requirements, that specify minimum performance levels. It also enables analytical expression of objectives, which are goals of the mission to be maximized. The

framework is generic and modular such that it is capable of supporting a variety of mission architectures and scenarios.

8.2.1 Model Elements

The four main elements of the framework are parameters, states, subsystems, and the schedule. Elements are constant or time-dependent, time notation is omitted for simplicity.

Parameters – A parameter, p , is a model input that provides numerical values to dynamically model system states and subsystem functions. Let P be the set of all model parameters, where $p \in P$. Examples parameters are orbital parameters, ground station locations, and T_f .

States – A system state is a model variable, and is defined as the information at some initial time that, combined with the input (parameters and the schedule) for all future time, uniquely determines the output for all future time [21]. Let $\mathbf{X} = [x_1, \dots, x_k, \dots x_m]^T$ be the vector of all the system state variables, where there are m variables. Example states include on-board resources such as energy and payload data. Opportunities for mission operations such as payload operation and ground station availability are also system states. An opportunity is modeled as binary, $o \in \{0, 1\}$, where a value of one indicates an opportunity and zero indicates no opportunity.

Subsystems – A subsystem, s , performs functions on states. Let S be the set of all subsystems. A single function operates on state k and is denoted $f_{s,j,k} \in F$, where $j \in J_s$ is the function index, and J_s is the set of all function indices. $f_{s,j,k}$ is an element of the set of functions, F .

Schedule – The schedule, $U(t)$, is a series of time-dependent events that describes how and when the subsystem functions operate on the states. Events are scheduled when there are opportunities. For example, a data download event may occurs when there is a line of sight between a ground station and satellite. The schedule is designed to achieve the mission objectives while satisfying the mission constraints. The schedule may be an output (e.g. when a solver is used to find an optimal schedule) or an input (e.g. when simulating a given schedule to test performance).

8.2.2 Framework Formulation

The model is formulated as a conventional optimization problem in Eqs. 8.1-8.4. Mission objectives, represented in Eq. 8.1, maximize the total transfer of a mission-specific system state, x^* , a component of \mathbf{X} , over the planning horizon. The decisions in the optimization problem are when and how the events occur, which are captured in the schedule, $U(t)$, which is an output of the optimization problem as formulated here. The constraints in the formulation include state dynamics (Eq. 8.2), bounds on state values (Eq. 8.3),

and mission requirements (Eq. 8.4).

$$\max_{U(t)} \{x^*(T_f)\} \quad (8.1)$$

s.t.

$$\mathbf{X}(t + \Delta t) = \mathbf{N}(\mathbf{X}, P, t) + \sum_{s \in S} \sum_{j \in J_s} \mathbf{F}_{s,j}(\mathbf{X}, U, P_{s,j}, t) \quad 0 \leq t \leq T_f \quad (8.2)$$

$$\mathbf{X}_{min} \leq \mathbf{X}(t) \leq \mathbf{X}_{max} \quad 0 \leq t \leq T_f \quad (8.3)$$

$$\Theta_{k,i} \leq \int_{t_i}^{t_{i+1}} x_k(t) dt \quad \forall x_k \in \mathbf{X}, i \in I_k \quad (8.4)$$

States evolve over time due to nominal dynamics and subsystem functions (see Eq. 8.2). Nominal dynamics are independent of subsystem functions. The vector of nominal dynamics equations is defined in Eq. 8.5, where each element k represents the nominal dynamics of state x_k . Orbital motion and battery self-discharge are example nominal dynamics of the state variables position and on-board energy, respectively.

$$\mathbf{N}(\mathbf{X}, P, t) = [n_1(\mathbf{X}, P, t), \dots, n_k(\mathbf{X}, P, t), \dots]^T, \quad (8.5)$$

The vector of subsystem functions that operates on the state vector is expressed in Eq. 8.6. The inputs to each function $f_{s,j,k}$ include the states, parameters, schedule, and time. Note the vector in Eq. 8.6 contains zero entries when combined subsystems and functions do not operate on specific states.

$$\mathbf{F}_{s,j}(\mathbf{X}, U, P_{s,j}, t) = [f_{s,j,1}(\mathbf{X}, U, P_{s,j}, t), \dots, f_{s,j,k}(\mathbf{X}, U, P_{s,j}, t), \dots]^T \quad \forall s \in S, j \in J_s \quad (8.6)$$

The nominal and functional dynamics in Eqs. 8.5 and 8.6 may each be described by any type of function, for example they may be analytical or extracted from a simulation system.

The state vector, \mathbf{X} , is constrained by lower and upper bounds, $\{\mathbf{X}_{min}, \mathbf{X}_{max}\} \in P$, as in Eq. 8.3. Example bounds include maximum and minimum battery capacity and maximum data storage capacity.

Operational mission requirements are represented in Eq. 8.4 by enforcing a minimum change in system state over a specific time period. For example, there may be a mission requirement that a minimum amount of state (such as energy) must be acquired or consumed during a certain period of time. Each interval $i \in I_k$, where I_k is the set of intervals spanning the full planning horizon for state x_k , has a start time, $0 \leq t_i \leq T_f$, where the end of interval i corresponds to the start of interval $i + 1$. Eq. 8.4 enforces a minimum change of state x_k during every interval $i \in I_k$, represented as $\Theta_{k,i}$. The change in state during interval i is its integrated time rate of change from t_i to t_{i+1} . For states without requirements, $\Theta_{k,i}$ will be zero $\forall i \in I_k$.

Another perspective for describing spacecraft operations is to consider subsystem functions individually. In particular, consider the analytical relationship between inputs and outputs specific to subsystem s and function j , $\mathbf{Z}_{s,j} = g_{s,j}(\mathbf{Y}_{s,j}, U, P, t)$, where the vector of inputs is $\mathbf{Y}_{s,j}$ and the vector of outputs is $\mathbf{Z}_{s,j}$, which are both comprised of components of \mathbf{X} . The function $g_{s,j}$ is the combination of $f_{s,j,k} \forall k \in K$, i.e., it models the impact of subsystem s and function j on all state inputs and outputs. These relationships for a single subsystem are shown in Figure 12.

8.2.3 Block Diagram Representation

We represent the model framework using a conventional control system block diagram to demonstrate the interaction of the various model elements in Figure 13. The set P of parameters is provided to the input block, which identifies opportunities for subsystem functions, O , and interprets the mission requirements,

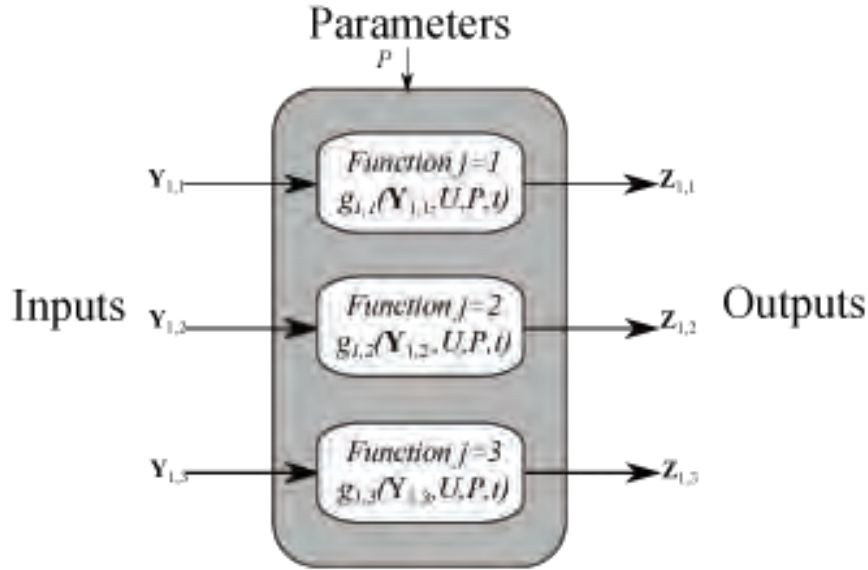


Figure 12: A generic representation of the subsystem function $Z_{s,j} = g_{s,j}(Y_{s,j}, U, P_{s,j}, t)$ for $s = 1$ and $j = 1, 2, 3$. All values are time dependent.

R, as control inputs. The error signal is expressed as $\mathbf{E} = \mathbf{R} - \mathbf{M}$, where \mathbf{M} is estimated state values, which are measured by on-board or ground sensors. \mathbf{E} , \mathbf{P} and \mathbf{R} are provided to the scheduler, which generates the operational schedule, U . Note that U is an output of the controller and an input to the dynamic system. The states evolve according to both the nominal dynamics and subsystem functions as prescribed by the U , where updated states (after time Δt) are denoted $\mathbf{X}(t + \Delta t)$. Unmodeled realistic disturbances, \mathbf{D} , may be injected into the system and modify the state. Mission performance is evaluated by measuring the states and verifying if the mission requirements are satisfied and comparing realized objectives to their expected values. Feedback control occurs when the scheduler updates U according to mission performance, i.e., uses \mathbf{E} in for future scheduling decisions.

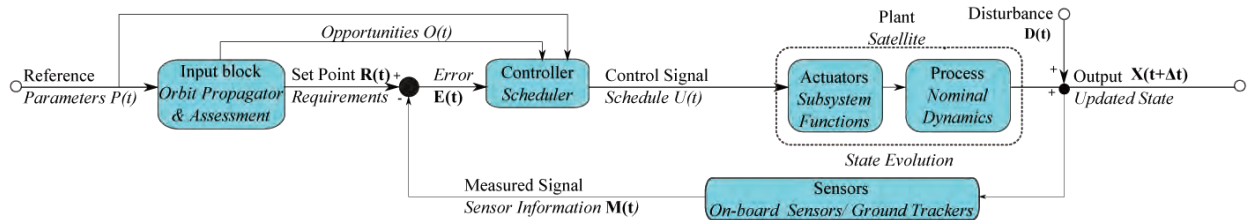


Figure 13: Elements and dynamics of the system model represented with a conventional feedback control loop diagram. The non-italicized labels are the conventional elements of a control feedback loop. The italicized labels are the elements of the modeling framework.

8.3 Research Plans

Thus far we developed a sophisticated model for space communication systems and developed an optimization algorithm for single-satellite, multiple ground station scheduling. Our next steps will include the following:

- Develop, model, implement and analyze a stochastic version of the single satellite, multiple ground station problem. Initial results will be reported later in the year.
- Develop concepts for multi-satellite and multi-ground station architectures.

References

- [1] R. A. Akmaev. Simulation of large-scale dynamics in the mesosphere and lower thermosphere with the doppler-spread parameterization of gravity waves: 2. eddy mixing and the diurnal tide. *Journal of Geophysical Research: Atmospheres (1984-2012)*, 106(D1):1205–1213, 2001.
- [2] A. A. Ali, A. Goel, A. J. Ridley, and D. S. Bernstein. Retrospective-Cost-Based Adaptive Input and State Estimation for the IonosphereThermosphere. *J. Aerospace Information Systems*, 2015. available online.
- [3] J. Anderson, T. Hoar, K. Raeder, H. Liu, N. Collins, R. Torn, and A. Arellano. The data assimilation research testbed. *Bul. Amer. Met. Soc.*, 90:1283–1296, 2009.
- [4] J. L. Anderson. An ensemble adjustment kalman filter for data assimilation. *Monthly Weather Review*, 129:2884–2903, 2001.
- [5] J. L. Anderson. An ensemble adjustment kalman filter for data assimilation. *Monthly Weather Review*, 129:2884–2903, 2001.
- [6] J. L. Anderson. Exploring the need for localization in ensemble data assimilation using an hierarchical ensemble filter. *Physica D*, 230:99–111, 2007.
- [7] J. L. Anderson. Spatially and temporally varying adaptive covariance inflation for ensemble filters. *Tellus*, 61:72–83, 2009.
- [8] Jeffrey L. Anderson. An ensemble adjustment Kalman filter for data assimilation. *Monthly Weather Review*, 129:2884–2903, 2001.
- [9] D. Angeli. A Lyapunov approach to incremental stability properties. *IEEE Trans. Autom. Control*, 47:410–421, 2002.
- [10] anonymous. CHAMP. <http://ilrs.gsfc.nasa.gov/satellitemissions/listofsatellites/chamgeneral.html>.
- [11] H. Bahcivan, M. C. Kelley, and J. W. Cutler. Radar and rocket comparison of uhf radar scattering from auroral electrojet irregularities: Implications for a nanosatellite radar. In *J. Geophys. Res.*, volume 114, A06309, 2009.
- [12] R. Bauske and G. W. Prölss. Modeling the ionospheric response to traveling atmospheric disturbances. *J. Geophys. Res.*, 102:14555, 1997.
- [13] H. Bekerat, R. Schunk, L. Scheirles, and A. Ridley. Comparison of satellite ion drift velocities with amie derived convection patterns. *J. Atmos. Sol-Terr. Phys.*, 67:1463–1479, 2005.
- [14] S. Bhattacharyya. Observer design for linear systems with unknown inputs. *IEEE Trans. Autom. Control*, 23:483–484, 1978.
- [15] P. Bournes and D. Williamson. (u) cubesat experiments (qbx). Presented at the 2009 Cubesat Developer's Workshop, April 2009.
- [16] G. Burgers, P. J. van Leeuwen, and G. Evensen. Analysis scheme in the ensemble kalman filter. *Monthly Weather Review*, 126:1719–1724, 1998.

- [17] A. G. Burns, T. L. Killeen, G. R. Carignan, and R. G. Roble. Large enhancements in the O/N₂ ratio in the evening sector of the winter hemisphere during geomagnetic storms. *J. Geophys. Res.*, 100:14661, August 1995. doi:10.1029/94JA03235.
- [18] A. G. Burrell, A. Goel, A. J. Ridley, and D. S. Bernstein. Correction of the photoelectron heating efficiency within the global ionosphere-thermosphere model using retrospective cost model refinement. *Journal Atmospheric and Solar-Terrestrial Physics*, 124:30–38, 2015.
- [19] J. Castaing, A. Cohn, and J. Cutler. Scheduling downloads for multi-satellite, multi-ground station missions. In *Proc. 28th Annual AIAA/USU Conference on Small Satellites*, Logan, UT, August 2014. SSC14-VIII-4.
- [20] P. C. Chamberlin, T. N. Woods, and F. G. Eparvier. Flare irradiance spectral model (fism): Daily component algorithms and results. *Space Weather*, 5:S07005, 2007. doi:10.1029/2007SW000316.
- [21] R. Chen, S. AhmadBeygi, D. Beil, A. Cohn, and A. Sinha. Solving truckload procurement auctions over an exponential number of bundles. *Transportation Science*, 43(4):493–510, November 2009.
- [22] James Cutler, Aaron Ridley, and Andrew Nicholas. Cubesat investigating atmospheric density response to extreme driving (cadre). In *Proceedings of the 25th Annual Small Satellite Conference*, Logan, UT, August 2011.
- [23] James W. Cutler, John C. Springmann, Sara Spangelo, and Hasan Bahcivan. Initial flight assessment of the radio aurora explorer. In *Proceedings of the 25th Annual Small Satellite Conference*, Logan, Utah, August 2011.
- [24] A. M. D’Amato, A. A. Ali, A. Ridley, and D. S. Bernstein. Retrospective cost optimization for adaptive state estimation, input estimation, and model refinement. In *Procedia Computer Science*, Vol. 18, *Proceedings of the ICCS*, pages 1919–1928, Barcelona, Spain, June 2013.
- [25] A. M. D’Amato, A. J. Ridley, and D. S. Bernstein. Retrospective-cost-based adaptive model refinement for the ionosphere and thermosphere. *Statistical Analysis and Data Mining*, 4:446–458, 2011.
- [26] A. M. D’Amato, J. Springmann, A. A. Ali, J. W. Cutler, A. J. Ridley, and D. S. Bernstein. Adaptive state estimation for nonminimum-phase systems with uncertain harmonic inputs. In *Proc. AIAA Guid. Nav. Contr. Conf.*, Portland, OR, August 2011. AIAA-2011-6315.
- [27] A. M. D’Amato, J. Springmann, A. A. Ali, J. W. Cutler, A. J. Ridley, and D. S. Bernstein. Adaptive state estimation for nonminimum-phase systems with uncertain harmonic inputs. In *Proc. AIAA Guid. Nav. Contr. Conf.*, Portland, OR, August 2011. AIAA-2011-6315.
- [28] A. M. D’Amato, E. D. Sumer, and D. S. Bernstein. Frequency-domain stability analysis of retrospective-cost adaptive control for systems with unknown nonminimum-phase zeros. In *Proc. Conf. Dec. Contr.*, pages 1098–1103, Orlando, FL, December 2011.
- [29] W. Deng, T.L. Killeen, A.G. Burns, and R.G. Roble. The flywheel effect: Ionospheric currents after a geomagnetic storm. *Geophys. Res. Lett.*, 18:1845, 1991.
- [30] Y. Deng, A. D. Richmond, A. J. Ridley, and H.-L. Liu. Assessment of the non-hydrostatic effect on the upper atmosphere using a general circulation model (gcm). *Geophys. Res. Lett.*, 35:L01104, 2008. doi:10.1029/2007GL032182.

[31] Y. Deng and A.J. Ridley. Dependence of neutral winds on interplanetary magnetic field, $F_{10.7}$ and hemispheric power index at high latitude. *J. Geophys. Res.*, 111:A09306, 2006. doi:10.1029/2005JA011368.

[32] C. L. Enloe, L. Habash Krause, R. K. Haaland, T. T. Patterson, C. E. Richardson, C. C. Lazidis, and R. G. Whiting. Miniaturized electrostatic analyzer manufactured using photolithographic etching. *Review of Scientific Instruments*, 74(3):1192–1195, 2003.

[33] G. Evensen. Sequential data assimilation with a nonlinear quasi-geostrophic model using monte carlo methods to forecast error statistics. *J. Geophys. Res.*, 99:10,143–10,162, 1994.

[34] X. Fang, C. E. Randall, D. Lummerzheim, W. Wang, G. Lu, S. C. Solomon, and R. A. Frahm. Parameterization of monoenergetic electron impact ionization. *Geophys. Res. Lett.*, 37:22106, 2010.

[35] T. T. Finne, A. C. Nicholas, C. Coker, S. A. Budzien, M. S. Johnson, S. P. Arnold, F. Herrero, M. G. McHarg, R. L. Balthazor, R. A. Doe, G. S. Bust, G. Crowley, and P. R. Straus. Small sensors for space weather: Cubesat missions poster. In *Eos Trans. AGU*, volume Abstract SM33C-1590, 2009.

[36] T. Floquet and J. P. Barbot. State and unknown input estimation for linear discrete-time systems. *Automatica*, 44:1883–1889, 2006.

[37] J.C. Foster, F.-P. St. Maurice, and V.J. Abreu. Joule heating at high latitudes. *J. Geophys. Res.*, 88:4885, 1983.

[38] R.A. Frahm, J.D. Winningham, J. R. Sharber, R. Link, G. Crowley, E. E. Gaines, D. L. Chenette, B. J. Anderson, and T. A. Potemra. The diffuse aurora: A significant source of ionization in the middle atmosphere. *J. Geophys. Res.*, 102:28203, 1997.

[39] S. Fukao, Yamanaka, D. Manabu, N. Ao, W. K. Hocking, T. Sato, M. Yamamoto, T. Nakamura, T. Tsuda, and S. Kato. Seasonal variability of vertical eddy diffusivity in the middle atmosphere: 1. three-year observations by the middle and upper atmosphere radar. *Journal of Geophysical Research: Atmospheres (1984-2012)*, 99(D9):18973–18987, 1994.

[40] T.J. Fuller-Rowell and D.S. Evans. Height-integrated Pedersen and Hall conductivity patterns inferred from TIROS–NOAA satellite data. *J. Geophys. Res.*, 92:7606, 1987.

[41] R. R. Garcia and S. Solomon. The effect of breaking gravity waves on the dynamics and chemical composition of the mesosphere and lower thermosphere. *Journal of Geophysical Research: Atmospheres (1984-2012)*, 90(D2):3850–3868, 1985.

[42] D.A. Hardy, M.S. Gussenhoven, R. Raistrick, and W.J. McNeil. Statistical and functional representation of the pattern of auroral energy flux, number flux, and conductivity. *J. Geophys. Res.*, 92:12,275, 1987.

[43] J.P. Heppner and N.C. Maynard. Empirical high-latitude electric field models. *J. Geophys. Res.*, 92:4467, 1987.

[44] F. A. Herrero, H. H. Jones, and J. G. Lee. The gated electrostatic mass spectrometer (gems): Definition and preliminary results. *Journal of the American Society for Mass Spectrometry*, 19(10):1384 – 1394, 2008.

[45] H.E. Hinteregger, K. Fukui, and B.R. Gibson. Observational, reference and model data on solar EUV from measurements on AE-E. *Geophys. Res. Lett.*, 8:1147, 1981.

[46] J. B. Hoagg and D. S. Bernstein. Retrospective cost model reference adaptive control for nonminimum-phase discrete-time systems, part 1: The adaptive controller; part 2: Stability analysis. In *Proc. Amer. Contr. Conf.*, pages 2927–2938, San Francisco, CA, June 2011.

[47] J. B. Hoagg and D. S. Bernstein. Retrospective cost model reference adaptive control for nonminimum-phase systems. *AIAA J. Guid. Contr. Dyn.*, 35:1767–1786, 2012.

[48] J. B. Hoagg, M. A. Santillo, and D. S. Bernstein. Discrete-time Adaptive Command Following and Disturbance Rejection with Unknown Exogenous Dynamics. *IEEE Trans. Autom. Contr.*, 53:912–928, 2008.

[49] M. Hou and P. Muller. Design of observers for linear systems with unknown inputs. *IEEE Trans. Autom. Control*, 37:871–875, 1992.

[50] P. L. Houtekamer and Herschel L. Mitchell. Data assimilation using an ensemble Kalman filter technique. *Monthly Weather Review*, 126:796–811, 1998.

[51] J. T. Hwang, D. Y. Lee, J. W. Cutler, and J. R. R. A. Martins. Large-Scale Multidisciplinary Optimization of a Small Satellites Design and Operation. *J. Spacecraft and Rockets*, 51:1648–1663, 2014.

[52] E. Kalnay, L. Hong, T. Miyoshi, S.-C. Yang, and J. Ballabrera-Poy. 4-var or ensemble kalman filter? *Tellus*, 59A:758–773, 2003.

[53] J. Kappenman. A perfect storm of planetary proportions. *IEEE Spectrum*, pages 26–31, February 2012.

[54] M.C. Kelley. *The Earth's Ionosphere*. Academic Press, Inc., San Diego, 1989.

[55] E. A. Kihn, R. Redmon, A. J. Ridley, and M. R. Hairston. A statistical comparison of the AMIE derived and DMSP-SSIES observed high-latitude ionospheric electric field. *J. of Geophys. Res.*, 111:8303, 2006.

[56] E.A. Kihn and A.J. Ridley. A statistical analysis of the amie auroral specification. *J. Geophys. Res.*, 110, 2005. A07305,10.1029/2004JA010775.

[57] T.L. Killeen and R.G. Roble. An analysis of the high-latitude thermospheric wind pattern calculated by a thermospheric general circulation model 1. Momentum forcing. *J. Geophys. Res.*, 89:7509, 1984.

[58] V. W. J. H. Kirchhoff and B. R. Clemesha. Eddy diffusion coefficients in the lower thermosphere. *Journal of Geophysical Research: Space Physics (1978-2012)*, 88(A7):5765–5768, 1983.

[59] S. Kirtikar, H. Palanthandlam-Madapusi, E. Zattoni, and D. S. Bernstein. l -delay input and initial-state reconstruction for discrete-time linear systems. *Circ. Sys. Sig. Processing*, 30:233–262, 2011.

[60] P. K. Kitanidis. Unbiased minimum-variance linear state estimation. *Automatica*, 23:775–778, 1987.

[61] D. Y. Lee, J. W. Cutler, J. Mancewicz, and A. J. Ridley. Maximizing photovoltaic power generation of a space-dart configured satellite. *Acta Astronautica*, 111:283–299, 2015.

[62] B. Lemay, J. Castaing, R. Zidek, A. Cohn, and J. Cutler. An Optimization-Based Approach for Small Satellite Download Scheduling, with Real-World Applications. submitted.

[63] H. Liu, J. Anderson, Y.-H. Kuo, C. Snyder, and A. Caya. Evaluation of a non-local observation operator in assimilation of champ radio occultation refractivity with wrf. *Monthly Weather Review*, 136:242–256, 2008.

[64] X. Liu and A. Ridley. A simulation study of the thermosphere mass density response to substorm using gitm model. *Journal of Geophysical Research: Space Physics*, 2015. submitted.

[65] A. M. Morozov, A. A. Ali, A. M. D’Amato, A. J. Ridley, S. L. Kukreja, and D. S. Bernstein. Retrospective-cost-based model refinement for system emulation and subsystem identification. In *Proc. Conf. Dec. Contr.*, pages 2142–2147, Orlando, FL, December 2011.

[66] A. V. Morozov, A. J. Ridley, D. S. Bernstein, N. Collins, T. J. Hoar, and J. L. Anderson. Data assimilation and driver estimation for the global ionosphere-thermosphere model using the ensemble adjustment kalman filter. *J. Atmospheric and Solar-Terrestrial Physics*, 104:126–136, 2013.

[67] Isaac Nason, Jordi Puig-Sair, and Robert J. Twiggs. Development of a family of picosatellite deployers based on the cubesat standard. In *Proceedings of IEEE Aerospace Conference*, Big Sky, Montana, 2002.

[68] National Research Council Canada. Dominion radio astrophysical observatory, 2012. [accessed 6-February-2013].

[69] P. T Newell, T Sotirelis, and S Wing. Diffuse, monoenergetic, and broadband aurora: The global precipitation budget. *J. Geophys. Res.*, 114:09207, 2009.

[70] R. Oehmke and Q. Stout. Parallel adaptive blocks on the sphere. In *Proc. 11th SIAM Conf. Parallel Processing for Scientific Computing*, SIAM, 2001.

[71] R.C. Oehmke. *High Performance Dynamic Array Structures*. PhD thesis, University of Michigan, 2004. Department of Electrical Engineering and Computer Science.

[72] H. J. Palanthandlam-Madapusi and D. S. Bernstein. Unbiased minimum-variance filtering for input reconstruction. In *Proc. Amer. Cont. Conf.*, pages 5712–5717, New York City, NY, 2007.

[73] L. Qian, S. C. Solomon, and T. J. Kane. Seasonal variation of thermospheric density and composition. *Journal of Geophysical Research: Space Physics (1978-2012)*, 114(A1), 2009.

[74] P. G. Richards, J. A. Fennelly, and D. G. Torr. EUVAC: A solar EUV flux model for aeronomics calculations. *J. Geophys. Res.*, 99:8981, 1994.

[75] A.D. Richmond. Assimilative mapping of ionospheric electrodynamics. *Adv. Space Res.*, 12:59, 1992.

[76] A.D. Richmond and Y. Kamide. Mapping electrodynamic features of the high-latitude ionosphere from localized observations: Technique. *J. Geophys. Res.*, 93:5741–5759, 1988.

[77] A. J. Ridley, Y. Deng, and G. Tóth. The global ionosphere-thermosphere model. *J. Atmos. Sol-Terr. Phys.*, 68:839–864, 2006.

[78] A. J. Ridley, J. M. Forbes, J. Cutler, A. C. Nicholas, J. P. Thayer, T. J. Fuller-Rowell, T. Matsuo, W. A. Bristow, M. G. Conde, D. P. Drob, L. J. Paxton, S. Chappie, M. Osborn, M. Dobbs, J. Roth, and Armada Mission Team. The Armada mission: Determining the dynamic and spatial response of the thermosphere/ionosphere system to energy inputs on global and regional scales. *American Geophysical Union (AGU) Fall Meeting*, pages A7+, December 2010.

[79] A.J. Ridley. Estimation of the uncertainty in timing the relationship between magnetospheric and solar wind processes. *J. Atmos. Sol-Terr. Phys.*, 62:757, 2000.

[80] A.J. Ridley and E.A. Kihn. Polar cap index comparisons with AMIE cross polar cap potential, electric field, and polar cap area. *Geophys. Res. Lett.*, 31, 2004.

[81] G. Russo, M. di Bernardo, and E. D. Sontag. Global entrainment of transcriptional systems to periodic inputs. *PLOS Computational Biology*, 6:1–26, 2010.

[82] M. A. Santillo and D. S. Bernstein. Adaptive control based on retrospective cost optimization. *AIAA J. Guid. Contr. Dyn.*, 33(2):289–304, 2010.

[83] M. N. Sasi and L. Vijayan. Turbulence characteristics in the tropical mesosphere as obtained by mst radar at gadanki (13.5 n, 79.2 e). *In Annales Geophysicae*, 19:1019–1025, 2001.

[84] J.R. Sharber, R.A. Frahm, J. D. Winningham, J. C. Biard, D. Lummerzheim, M. H. Rees, D. L. Chenette, E. E. Gaines, R. W. Nightingale, and W. L. Imhof. Observations of the UARS particle environment monitor and computation of ionization rates in the middle and upper atmosphere during a geomagnetic storm. *Geophys. Res. Lett.*, 20:1319, 1993.

[85] Eduardo Sontag. Contractive systems with inputs. In Jan C. Willems, Shinji Hara, Yoshito Ohta, and Hisaya Fujioka, editors, *Perspectives in Mathematical System Theory, Control, and Signal Processing*, volume 398, pages 217–228. Springer, 2010.

[86] S. Spangelo, D. Boone, and J. W. Cutler. Assessing the capacity of a federated ground station network. In *Proceedings of IEEE Aerospace Conference*, Big Sky, Montana, 2010.

[87] S. Spangelo, J. Cutler, K. Gilson, and A. Cohn. Optimization-Based Scheduling for the Single-Satellite, Multi-Ground Station Communication Problem. *Computers and Operations Research*, 57:1–16, 2015.

[88] S. Spangelo and J. W. Cutler. Small Satellite Operations Model to Assess Data and Energy Flows. *AIAA/AAS Astrodynamics Specialist Conference Proceedings*, 2010.

[89] J. C. Springmann. Attitude-independent magnetometer calibration with time-varying bias. In *Proceedings of the 25th Annual Small Satellite Conference*, Logan, UT, August 2011.

[90] J. C. Springmann and J. W. Cutler. On-orbit calibration of photodiodes for attitude determination. In *Proceedings of the 27th Annual AIAA/USU Small Satellite Conference*, Logan, UT, August 2013. SSC13-VIII-1.

[91] A. W. Stephan, R. R. Meier, and L. J. Paxton. Comparison of Global Ultraviolet Imager limb and disk observations of column O/N_2 during a geomagnetic storm. *J. Geophys. Res.*, 113:1301, 2008. doi:10.1029/2007JA012599.

[92] D.J. Strickland, R.J. Cox, R.R. Meier, and D.P. Drob. Global O/N_2 derived from DE-1 FUV dayglow data: Technique and examples from two storm periods. *J. Geophys. Res.*, 103:4251, 1998.

[93] E. D. Sumer, A. M. D’Amato, A. M. Morozov, J. B. Hoagg, and D. S. Bernstein. Robustness of retrospective cost adaptive control to markov-parameter uncertainty. In *Proc. Conf. Dec. Contr.*, pages 6085–6090, Orlando, FL, December 2011.

[94] S. Sundaram and C. N. Hadjicostis. Delayed observers for linear systems with unknown inputs. *IEEE Trans. Autom. Control*, 52:334–339, 2007.

- [95] W. K. Tobiska. Current status of solar EUV measurements and modeling. *Adv. Space Res.*, 18:3–10, 1996.
- [96] M. E. Valcher. State observers for discrete-time linear systems with unknown inputs. *IEEE Trans. Autom. Control*, 44:397–401, 1999.
- [97] D.R. Weimer. A flexible, IMF dependent model of high-latitude electric potential having "space weather" applications. *Geophys. Res. Lett.*, 23:2549, 1996. doi:10.1029/2000JA000604.
- [98] T. N. Woods, F. G. Eparvier, S. M. Bailey, P. C. Chamberlin, J. Lean, G. J. Rottman, S. C. Solomon, W. K. Tobiska, and D. L. Woodraska. Solar EUV Experiment (SEE): Mission overview and first results. *J. Geophys. Res.*, 110:1312–+, 2005.
- [99] T.N. Woods et al. Xuv photometer system (xps): Improved solar irradiance algorithm using chianti spectral models. *Solar Phys.*, 249:235–267, 2008.
- [100] T.N. Woods and G.J. Rottman. Solar ultraviolet variability over time periods of aeronomical interest. *Atmospheres in the Solar System: Comparative Aeronomy, Geophys. Monogr. Ser.*, 130:221, 2002.
- [101] Y. Xiong and M. Saif. Unknown disturbance inputs estimation based on a state functional observer design. *Automatica*, 39:1389–1398, 2003.

1.

1. Report Type

Final Report

Primary Contact E-mail

Contact email if there is a problem with the report.

dsbaero@umich.edu

Primary Contact Phone Number

Contact phone number if there is a problem with the report

7347643719

Organization / Institution name

University of Michigan

Grant/Contract Title

The full title of the funded effort.

Transformative Advances in DDDAS with Application to Space Weather Monitoring

Grant/Contract Number

AFOSR assigned control number. It must begin with "FA9550" or "F49620" or "FA2386".

FA9550-12-1-0401

Principal Investigator Name

The full name of the principal investigator on the grant or contract.

Dennis S. Bernstein

Program Manager

The AFOSR Program Manager currently assigned to the award

Frederica Darema

Reporting Period Start Date

09/01/2012

Reporting Period End Date

10/14/2015

Abstract

This project focused on DDDAS-motivated developments in support of space weather monitoring and prediction. The project involved four interrelated tasks relating to physics-driven adaptive modeling, adaptive

data assimilation with input reconstruction, event-based sensor reconfiguration, and optimization of scheduling. For data assimilation, the emphasis has been on model refinement. The problem of estimating the eddy diffusion coefficient using total electron content measurements has led to new techniques for determining the essential modeling details needed by the retrospective cost model refinement technique. For spacecraft design, multidisciplinary optimization design techniques were applied to the design of small satellites accounting for multiple vehicle subsystems. For download scheduling, optimization techniques were used to account for multiple spacecraft and ground stations.

Distribution Statement

This is block 12 on the SF298 form.

Distribution A - Approved for Public Release

Explanation for Distribution Statement

If this is not approved for public release, please provide a short explanation. E.g., contains proprietary information.

DISTRIBUTION A: Distribution approved for public release.

SF298 Form

Please attach your [SF298](#) form. A blank SF298 can be found [here](#). Please do not password protect or secure the PDF. The maximum file size for an SF298 is 50MB.

[AFD-070820-035DDDAS.pdf](#)

Upload the Report Document. File must be a PDF. Please do not password protect or secure the PDF . The maximum file size for the Report Document is 50MB.

[DDDASFinalReportVSept282015.pdf](#)

Upload a Report Document, if any. The maximum file size for the Report Document is 50MB.

Archival Publications (published) during reporting period:

A. A. Ali, A. Goel, A. J. Ridley, and D. S. Bernstein. Retrospective-Cost-Based Adaptive Input and State Estimation for the Ionosphere-Thermosphere. *J. Aerospace Information Systems*, 2015. available online.

A. G. Burrell, A. Goel, A. J. Ridley, and D. S. Bernstein. Correction of the photoelectron heating efficiency within the global ionosphere-thermosphere model using retrospective cost model refinement. *Journal Atmospheric and Solar-Terrestrial Physics*, 124:30–38, 2015.

J. Castaing, A. Cohn, and J. Cutler. Scheduling downloads for multi-satellite, multi-ground station missions. In *Proc. 28th Annual AIAA/USU Conference on Small Satellites*, Logan, UT, August 2014. *SSC14-VIII-4*.

James Cutler, Aaron Ridley, and Andrew Nicholas. Cubesat investigating atmospheric density response to extreme driving (cadre). In *Proceedings of the 25th Annual Small Satellite Conference*, Logan, UT, August 2011.

James W. Cutler, John C. Springmann, Sara Spangelo, and Hasan Bahcivan. Initial flight assessment of the radio aurora explorer. In *Proceedings of the 25th Annual Small Satellite Conference*, Logan, Utah, August 2011.

A. M. D'Amato, A. A. Ali, A. Ridley, and D. S. Bernstein. Retrospective cost optimization for adaptive state estimation, input estimation, and model refinement. In *Procedia Computer Science*, Vol. 18, *Proceedings of the ICCS*, pages 1919–1928, Barcelona, Spain, June 2013.

J. T. Hwang, D. Y. Lee, J. W. Cutler, and J. R. R. A. Martins. Large-Scale Multidisciplinary Optimization of a Small Satellites Design and Operation. *J. Spacecraft and Rockets*, 51:1648–1663, 2014.

D. Y. Lee, J. W. Cutler, J. Mancewicz, and A. J. Ridley. Maximizing photovoltaic power generation of a space-dart configured satellite. *Acta Astronautica*, 111:283–299, 2015.

A. V. Morozov, A. J. Ridley, D. S. Bernstein, N. Collins, T. J. Hoar, and J. L. Anderson. Data assimilation and driver estimation for the global ionosphere-thermosphere model using the ensemble adjustment kalman filter. *J. Atmospheric and Solar-Terrestrial Physics*, 104:126–136, 2013.

S. Spangelo, J. Cutler, K. Gilson, and A. Cohn. Optimization-Based Scheduling for the Single-Satellite, Multi-Ground Station Communication Problem. *Computers and Operations Research*, 57:1–16, 2015.

Changes in research objectives (if any):

None

Change in AFOSR Program Manager, if any:

None

Extensions granted or milestones slipped, if any:

None

AFOSR LRIR Number

LRIR Title

Reporting Period

Laboratory Task Manager

Program Officer

Research Objectives

Technical Summary

Funding Summary by Cost Category (by FY, \$K)

	Starting FY	FY+1	FY+2
Salary			
Equipment/Facilities			
Supplies			
Total			

Report Document

Report Document - Text Analysis

Report Document - Text Analysis

Appendix Documents

2. Thank You

E-mail user

Sep 28, 2015 10:27:04 Success: Email Sent to: dsbaero@umich.edu